



ELSEVIER

Contents lists available at ScienceDirect

Journal of Fluids and Structures

journal homepage: www.elsevier.com/locate/jfs

Suppression of vortex-induced vibrations by fairings: A numerical study



Yue Yu^{a,b}, Fangfang Xie^c, Hongmei Yan^d, Yiannis Constantinides^d,
Owen Oakley^e, George Em Karniadakis^{b,*}

^a Department of Mathematics, Lehigh University, Bethlehem, PA 18015, USA

^b Division of Applied Mathematics, Brown University, Providence, RI 02912, USA

^c Department of Mechanical Engineering, MIT, Cambridge, MA 02139, USA

^d Chevron Energy Technology Company, Houston, TX 77002, USA

^e Consultant, USA

ARTICLE INFO

Article history:

Received 4 December 2013

Accepted 19 January 2015

Available online 12 March 2015

Keywords:

Spectral element method

VIV

FSI

Partitioned method

Fictitious method

ABSTRACT

Fairings are nearly neutrally buoyant devices, fitted along the axis of long circular risers to suppress vortex-induced vibrations (VIV) and possibly reduce the drag force. Here we study numerically how VIV can be practically eliminated by using free-to-rotate fairings. Since the rotational inertia is low for the fairings, direct numerical simulations based on standard fluid–structure interaction algorithms may fail because of the so-called added mass effect. To resolve this problem we introduce fictitious methods and successfully stabilize the simulations. We then investigate the effect of rotational friction C_f on the stabilization effect of the fairings. In particular through two-dimensional (2D) simulations we find that when the Reynolds number is low ($Re=100$), $C_f=0$ is the most effective choice in suppressing VIV. Moreover, at this low Reynolds number there exists a critical value of C_f around which large oscillations and non-symmetric trajectories are observed. On the other hand, at higher Reynolds number ($Re=500$) a different behavior emerges, i.e. VIV are suppressed continuously as C_f increases. At $Re=1000$, we perform 3D simulations to investigate the effects of three-dimensionality of the flow on the vibration and rotation responses. In this work we quantify numerically for the first time various salient features of free-to-rotate devices for VIV suppression and relate them to modified flow structures in the near wake.

© 2015 Elsevier Ltd. All rights reserved.

1. Introduction

In deepwater offshore oil operations, riser interference and vortex-induced vibrations (VIV) are severe problems for risers, umbilicals and tendons in areas of strong currents. Such industry demands have greatly motivated the investigations of various methods for suppressing vortex-induced vibrations either experimentally (Cimbala and Garg, 1991; Owen et al., 2001; Assi et al., 2009, 2010, 2011; Korkischko and Meneghini, 2010) or numerically (Dong et al., 2008; Baek and Karniadakis, 2009), over the past decades. In theory, an effective VIV suppression device should not only eliminate the

* Corresponding author.

E-mail addresses: Yue_Yu_1@brown.edu (Y. Yu), xieff@mit.edu (F. Xie), hmyan@chevron.com (H. Yan), ycon@chevron.com (Y. Constantinides), hoakley@alum.mit.edu (O. Oakley), George_Karniadakis@brown.edu (G.E. Karniadakis).

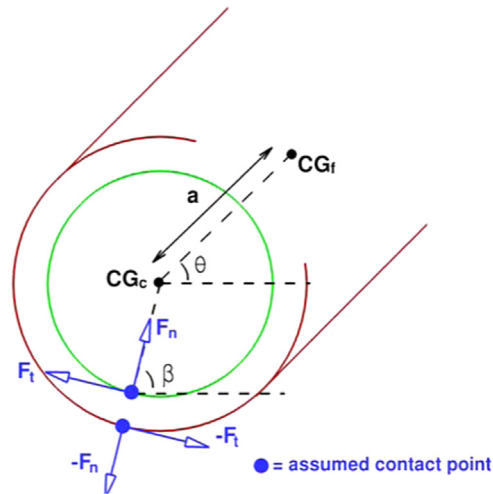


Fig. 1. Coordinate system and symbol definition for fairing and cylinder motions. Here we use green to represent the cylinder and red to represent the fairing, while the contact forces are marked by blue. (For interpretation of the references to color in this figure caption, the reader is referred to the web version of this article.)

vortex shedding, but also help in reducing the drag force thereby resolving the concern of the loads caused by strong currents. To get a comprehensive review of solutions for VIV suppression, we refer the readers to the works of Zdravkovich (1981) and Every et al. (1982) and the references therein. Among all these VIV suppression solutions, free-to-rotate suppressors such as splitter plates and fairings with different shapes are widely studied and employed to mitigate VIV and avoid interference as they reduce both drag forces and VIV (Cimbala and Garg, 1991; Assi et al., 2009, 2011). Assi et al. (2009) found that with a pair of parallel plates installed on the sides of the cylinder, the maximum VIV suppression and drag reduction occurred, and the level of rotational friction between the fairing and the cylinder played an important role. Specifically, the rotational damping and friction needs to be high enough to stabilize the device and achieve a better suppression performance. This requirement draws attention to the importance of parametric studies in fairing design and analysis. Hence, the critical parameters for fairing stability and performance need to be identified, and the effects of varying Reynolds number needs to be investigated. However, experimentally the hydrodynamic performance evaluation for fairings is done by tank testing, which is expensive and very difficult to find model basis availability. On the other hand, although the rotational friction is found to be a critical factor in the fairing effectiveness, it is difficult to determine it in the experimental tests. Therefore, computational fluid dynamics (CFD) can be employed as a helpful tool for fairing design and analysis, because it avoids schedule issues with testing, reduces the cost of testing, and provides possibilities of investigating the effect of varying rotational friction. In the present work we will contribute to the understanding of a type of fairing (see Fig. 1) employed in industry, by running fluid–structure interaction (FSI) simulations with our general purpose spectral element solver NEKTAR. To the authors' best knowledge, this is the first thorough numerical study of the VIV suppressing performances for varying rotational damping and friction coefficients, and also for a fairing with a pair of parallel plates attached. In the real world applications, the Reynolds number is higher than 10 000, hence requiring careful treatments and also large computational costs in CFD. To gain some insights on the fairing effectiveness while keeping the computational model simple, in this paper we will focus primarily on low Reynolds cases ($Re=100$ and 500), which can be simulated as two-dimensional problems. To evaluate the three-dimensional effects, we also conduct 3D simulations for the case $Re=1000$, which reveals similar trends as the ones observed in 2D simulations at $Re=500$.

In the numerical simulations, we are going to adopt the partitioned method where the fluid–structure interaction system is split into separate fluid and structure solvers, because of its better computational scalability and software modularity. However, the partitioned procedure in the fairing simulations is problematic, because of the so-called added-mass effect (Causin et al., 2005). Especially when the structure is light, or when the fairing has low rotational inertia, the added-mass effect becomes stronger and severely affects the stability of the fluid–structure interaction (FSI) procedure. To resolve these instabilities, a strong coupling is required to impose continuity at the interface at each time step. A number of approaches have been developed more recently to accelerate the convergence of the partitioned algorithm, including the Robin-Robin scheme (Astorino et al., 2009; Badia et al., 2008; Roux and Geraud, 2009), the interface artificial compressibility (Degroote et al., 2010, 2011), the stabilized explicit method (Burman and Fernández, 2007, 2009), and our fictitious methods (Baek and Karniadakis, 2012; Yu et al., 2013). In this work, we will adopt and generalize the fictitious methods, by developing a similar modified governing equation for the fairing rotational equation. In this new *fictitious inertia method*, additional acceleration terms are introduced in the structure solver to balance the added-mass effect caused by low rotational inertia and to provide further stabilization for problems with large fairing rotations.

The paper is organized as follows. In Section 2 we describe the FSI governing equations and discretization methods; firstly the governing equations of cylinder and fairing models are derived in Section 2.1 from conservation laws; then the

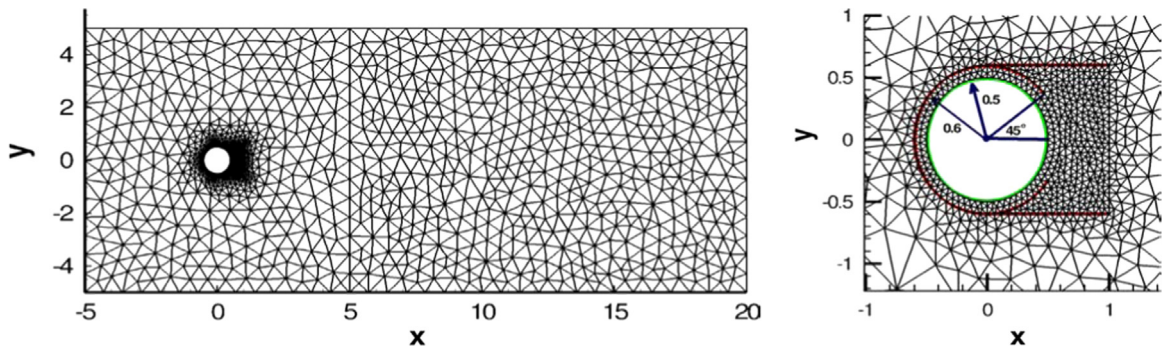


Fig. 2. Left: mesh and geometry for fluid solver, in the smaller domain simulations. Right: detailed mesh near the fairing and cylinder and structure geometries; here we use green to represent the cylinder and red to represent the fairing. (For interpretation of the references to color in this figure caption, the reader is referred to the web version of this article.)

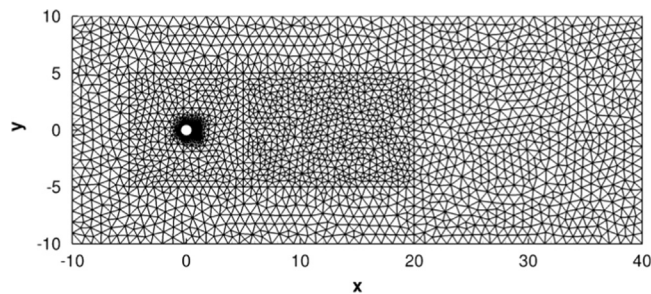


Fig. 3. Fluid mesh in the larger domain simulations.

numerical methods for the fluid and solid models are described in [Sections 2.2.1](#) [Sections 2.2.2](#), respectively; lastly, in [Section 2.3](#) we introduce the fictitious inertia method in the solid model, and summarize the FSI coupling procedure at each time step for the full partitioned algorithm. Various tests are performed in [Section 3](#) to investigate the related numerical issues as well as to validate the numerical method. To demonstrate the effect of our method and investigate the optimal fictitious coefficient, in [Section 3.1](#) we apply the fictitious method with varying coefficients, and compare the averaged subiteration numbers required for each time step. In [Section 3.2](#), elements with different polynomial orders are employed, to study the grid convergence of the spectral element method. With the optimal fictitious coefficients, in [Section 4](#) we provide a thorough parametric study on the fairings, with emphasis on their performances in VIV suppression and drag force reduction. The critical parameters for fairing stability and performance, i.e., the rotational damping and friction, are identified with two-dimensional (2D) simulations at $Re=100$ and $Re=500$, and with three-dimensional (3D) simulations at $Re=1000$. For the later case, the 2D and 3D simulation results are also compared to investigate the 3D effect. We end in [Section 5](#) with a brief summary. Additional details on the expression for friction between the cylinder and fairing are derived in the appendix.

2. Formulation

In this section we will describe the formulation for VIV of a rigid, spring mounted cylinder, which is covered with fairings as shown in [Fig. 1](#). The cylinder is free to respond in both cross-flow and stream-wise directions. The fairing moves following the cylinder, with an additional degree of freedom because it can rotate around the cylinder axis subjected to the hydrodynamic torque. The equations for fairing and cylinder motions will be derived, and our fluid–structure interaction procedure with fictitious methods will be employed to solve these equations. The geometry and mesh used in the following derivations and simulations are shown in [Figs. 2](#) and [3](#). To be more specific, the flow is simulated in two 2D domains: a smaller domain $[-5, 20] \times [-5, 5]$ for $Re=100$ and $Re=500$, and a larger domain $[-10, 40] \times [-10, 10]$ for $Re=500$ and $Re=1000$. For $Re=1000$ case, 3D simulations are also conducted on an extruded 2D domain $[-10, 40] \times [-10, 10] \times [0, 3]$. A solid cylinder of radius 0.5 is placed at the origin with a fairing surrounding the cylinder. At the inlet, a uniform steady flow with $U_\infty = 1$ is imposed, and at the outlet we employ zero Neumann boundary condition. Along the crossflow direction, a periodic boundary condition is applied. Therefore, we are simulating the motions of an array of cylinders which are arranged in the crossflow direction. The domain in [Fig. 2](#) is of length 10 in the y direction, which yields a gap size between each two neighboring cylinders as 10, while the larger domain in [Fig. 3](#) gives a larger gap of size 20. Here we adopt a fairing geometry as suggested in the industrial use: the fairing is composed by two parts: firstly the circular body part, which covers $\frac{3}{4}$ of the cylinder and centered at the cylinder center with radius 0.6; the other part is a pair of parallel plates attached to the top and

bottom points of the fairing circular part (see the red part in Fig. 1). As shown in the right plot of Fig. 2, in the initial configuration the plates are parallel to the stream-wise direction, with a length of 1.0, i.e., one cylinder diameter D . The mass on fairing is assumed to be evenly distributed, and therefore in the initial configuration the fairing's center of gravity locates at $(0.085, 0)$.

2.1. Cylinder and fairing models

The cylinder is assumed to be subjected to vortex-induced vibration with two degrees of freedom (DOF) in the (x, y) plane. The fairing is in contact with the cylinder and is free to rotate. There is a small gap between the fairing and cylinder with a single point of contact, where the fairing is pressed against the cylinder. As shown in Fig. 1, the system allows body motions with five degrees of freedom, including the cylinder's horizontal and vertical motions (c_x and c_y), and the fairing's horizontal, vertical motions (f_x and f_y) and rotational angle (θ). Here we define the following symbols to be used in the equations of motions:

- CG_c, CG_f : gravity center of cylinder and fairing, respectively.
- a : distance from CG_c to CG_f .
- f_c : coefficient of friction between the cylinder and fairing.
- F_{chx}, F_{chy} : hydrodynamic force applied on the cylinder in the x and y directions, respectively.
- k_x, k_y : cylinder spring constant in the x and y directions, respectively.
- F_{fmx}, F_{fmy} : hydrodynamic force applied on the fairing in the x and y directions, respectively.
- I_f : fairing rotational inertia about CG_f .
- m_c, m_f : mass of cylinder and fairing, respectively.
- M_{fh} : hydrodynamic angular momentum applied on the fairing about CG_f .
- R : cylinder radius.
- β : contact angle.
- F_n : cylinder-fairing normal contact force.
- F_t : cylinder-fairing tangential contact force.

To derive the equations of motions for the cylinder and fairing, we make the following assumptions:

1. There is no damping from the structure in translational and rotational directions.
2. The cylinder and the fairing are always in touch and have only one contact point.
3. The tangential contact Force F_t between the cylinder and the fairing is related to the normal contact force F_n following $F_t = f_c F_n$, where f_c is proportional to the sign function of $\partial\theta/\partial t$ with a constant sliding friction coefficient C_f , i.e.,

$$f_c = C_f \operatorname{sgn}\left(\frac{d\theta}{dt}\right). \quad (2.1)$$

Here C_f can be seen as an index for the rotational damping and friction. More details about this formula are provided in Appendix A.

Based on these assumptions, the equations of motions for the *cylinder* are written about CG_c :

$$\begin{aligned} m_c \frac{\partial^2 c_x}{\partial t^2} + k_x c_x - F_n (\cos \beta + f_c \sin \beta) &= F_{chx}, \\ m_c \frac{\partial^2 c_y}{\partial t^2} + k_y c_y - F_n (\sin \beta - f_c \cos \beta) &= F_{chy}, \end{aligned} \quad (2.2)$$

and the equations of motions for the *fairing* are written about CG_f :

$$\begin{aligned} m_f \frac{\partial^2 f_x}{\partial t^2} + F_n (\cos \beta + f_c \sin \beta) &= F_{fmx}, \\ m_f \frac{\partial^2 f_y}{\partial t^2} + F_n (\sin \beta - f_c \cos \beta) &= F_{fmy}. \end{aligned} \quad (2.3)$$

From Fig. 1 we can see that the gravity centers of the cylinder and fairing are geometrically related as

$$\begin{aligned} c_x &= f_x - a \cos \theta, \\ c_y &= f_y - a \sin \theta. \end{aligned} \quad (2.4)$$

Substituting these expressions into (2.2), the equations of motion for cylinder become

$$m_c \left[\frac{\partial^2 f_x}{\partial t^2} + a \left(\left(\frac{\partial \theta}{\partial t} \right)^2 \cos \theta + \frac{\partial^2 \theta}{\partial t^2} \sin \theta \right) \right] + k_x [f_x - a \cos \theta] - F_n (\cos \beta + f_c \sin \beta) = F_{chx},$$

$$m_c \left[\frac{\partial^2 f_y}{\partial t^2} + a \left(\left(\frac{\partial \theta}{\partial t} \right)^2 \sin \theta - \frac{\partial^2 \theta}{\partial t^2} \cos \theta \right) \right] + k_y [f_y - a \sin \theta] - F_n (\sin \beta - f_c \cos \beta) = F_{chy}. \quad (2.5)$$

In addition, we can derive another equation from the conservation of angular momentum. The total angular momentum $I_f \ddot{\theta}$ about CG_f should be equivalent to the resultant angular momentum exerted by cylinder-fairing contact force and the hydrodynamic angular momentum M_{fh} from the fluid. To be more specific, the torque of the cylinder-fairing normal contact force F_n about CG_f is $a \sin(\beta - \theta)$, and the torque of the cylinder-fairing tangential contact force F_t is $-(a \cos(\beta - \theta) + R)$. Therefore, we have the resultant angular momentum as

$$M_{fh} + F_n a \sin(\beta - \theta) - F_t (a \cos(\beta - \theta) + R).$$

By substituting the relation $F_t = f_c F_n$, the conservation of angular momentum can be expressed as

$$I_f \frac{\partial^2 \theta}{\partial t^2} - F_n [a \sin(\beta - \theta) - a f_c \cos(\beta - \theta) - R f_c] = M_{fh}. \quad (2.6)$$

Combining the equations of motion for the fairing (2.3) and the equations for cylinder (2.5), we obtain a system with 5 equations consisting of 5 unknowns ($f_x, f_y, \theta, \beta, F_n$):

$$m_c \left[\frac{\partial^2 f_x}{\partial t^2} + a \left(\left(\frac{\partial \theta}{\partial t} \right)^2 \cos \theta + \frac{\partial^2 \theta}{\partial t^2} \sin \theta \right) \right] + k_x [f_x - a \cos \theta] - F_n (\cos \beta + f_c \sin \beta) = F_{chx}, \quad (2.7a)$$

$$m_c \left[\frac{\partial^2 f_y}{\partial t^2} + a \left(\left(\frac{\partial \theta}{\partial t} \right)^2 \sin \theta - \frac{\partial^2 \theta}{\partial t^2} \cos \theta \right) \right] + k_y [f_y - a \sin \theta] - F_n (\sin \beta - f_c \cos \beta) = F_{chy}, \quad (2.7b)$$

$$m_f \frac{\partial^2 f_x}{\partial t^2} + F_n (\cos \beta + f_c \sin \beta) = F_{fhx}, \quad (2.7c)$$

$$m_f \frac{\partial^2 f_y}{\partial t^2} + F_n (\sin \beta - f_c \cos \beta) = F_{fhy}, \quad (2.7d)$$

$$I_f \frac{\partial^2 \theta}{\partial t^2} - F_n [a \sin(\beta - \theta) - a f_c \cos(\beta - \theta) - R f_c] = M_{fh}. \quad (2.7e)$$

2.2. Fluid–structure interaction

The right hand sides in the governing equations (2.7) for cylinder and fairing indicate that the motions of cylinder and fairing are subjected to the hydrodynamic forces and hydrodynamic angular momentum. On the other hand, the motions of cylinder and fairing in turn change the fluid domain and the boundary conditions. Therefore, this is a coupled fluid–structure interaction problem whose domain Ω is composed of two parts: the fluid subdomain $\Omega_f(t)$ occupied by the fluid, and the structure subdomain Ω_s occupied by the cylinder and fairing. There is a common boundary between the two subdomains, which is the fluid–structure interface $\Sigma(t) = \Omega_f(t) \cap \Omega_s$. For the structure kinematics we solve the system (2.7) with the Newton–Raphson procedure. On the other hand, the fluid problem is solved with the spectral element solver NEKTAR (Karniadakis and Sherwin, 2005). The Navier–Stokes equation is stated in an arbitrary Lagrangian–Eulerian framework (Hughes et al., 1981) since the fluid domain is changing with the movement of the cylinder and fairing. Roughly speaking, we aim to solve for three sets of variables in this FSI system: the fluid velocity $\mathbf{u}(\mathbf{x}, t)$, the fluid mesh velocity $\mathbf{w}(\mathbf{x}, t)$, and the 5 structure unknowns ($f_x, f_y, \theta, \beta, F_n$). Here $\mathbf{x} = \mathbf{x}(t)$ and \mathbf{X} are the position vectors in the deformed configuration and initial configuration, respectively. In the current work, we will use the partitioned procedure as employed by Baek and Karniadakis (2012) and Yu et al. (2013) to solve the fluid–structure interaction problem. To ensure the continuity on the interface, subiterations are employed at each time step. In the following Sections, we will denote the subiteration number by the subscript k , and the time step number by the superscript n .

2.2.1. Fluid solver

In the fluid model we employ the incompressible Navier–Stokes equation:

$$\frac{\partial \mathbf{u}}{\partial t} + (\mathbf{u} - \mathbf{w}) \cdot \nabla \mathbf{u} = -\frac{\nabla p}{\rho_f} + \nu \nabla^2 \mathbf{u} \quad \text{in } \Omega_f(t), \quad (2.8a)$$

$$\nabla \cdot \mathbf{u} = 0 \quad \text{in } \Omega_f(t), \quad (2.8b)$$

combined with the initial condition

$$\mathbf{u}(\mathbf{x}, t = 0) = \mathbf{u}_0(\mathbf{x}) \quad \text{in } \Omega_f(0), \quad (2.9)$$

and the Dirichlet boundary conditions on the interface, i.e.,

$$\mathbf{u} = \frac{\partial \boldsymbol{\eta}}{\partial t} \quad \text{on } \Sigma(t), \quad (2.10)$$

which enforces the continuity of velocities. Here, \mathbf{w} , p , ρ_f , and ν stand for the mesh velocity, pressure, fluid density, and the kinematic viscosity, respectively; $\boldsymbol{\eta}$ is the displacement of the specific point at the cylinder or fairing surface, which can be calculated from the structure simulation results as

$$\boldsymbol{\eta}(\mathbf{x}, t) = \begin{cases} \begin{pmatrix} c_x(t) \\ c_y(t) \end{pmatrix} + \mathbf{X} & \text{on cylinder,} \\ \begin{pmatrix} c_x(t) \\ c_y(t) \end{pmatrix} + \begin{pmatrix} \cos \theta(t) & -\sin \theta(t) \\ \sin \theta(t) & \cos \theta(t) \end{pmatrix} \mathbf{X} & \text{on fairing.} \end{cases} \quad (2.11)$$

At each time step, the mesh position \mathbf{x} will be obtained from the integration of the mesh velocity. To generate the mesh velocity \mathbf{w} , we define a “lifting” from the structure displacement on the interface: given the displacement on the interface $\boldsymbol{\eta}|_{\Sigma}$, we employ a harmonic extension mapping from the initial fluid configuration $\Omega_f(0)$ to the current configuration $\Omega_f(t)$. The mesh velocity \mathbf{w} satisfies

$$\nabla^2 \mathbf{w} = 0 \quad \text{in } \Omega_f(t), \quad (2.12a)$$

$$\mathbf{w} = \frac{\partial \boldsymbol{\eta}}{\partial t} \quad \text{on } \Sigma(t), \quad (2.12b)$$

which is endowed with vanishing boundary conditions on the other boundaries:

$$\mathbf{w} = 0 \quad \text{in } \partial\Omega_f(t) \setminus \Sigma(t). \quad (2.13)$$

To solve Eqs. (2.8) and (2.12) numerically, we employ the Navier–Stokes solver NEKTAR (Karniadakis and Sherwin, 2005) in which the spectral element method with Jacobi polynomial basis is used to represent the fluid velocity, fluid pressure and mesh velocity. To integrate in time, we use a high-order splitting scheme with three parts: first the nonlinear terms are treated explicitly, then the pressure is obtained by a Poisson equation solver, and finally the viscous terms are treated implicitly (Karniadakis et al., 1991). In the strongly coupled FSI system, at time step n and subiteration step k , we solve for \mathbf{u}_k^n and p_k^n from previous time step results \mathbf{u}^{n-i} and previous subiteration solution \mathbf{u}_{k-1}^n (Baek and Karniadakis, 2011):

$$\frac{\tilde{\mathbf{u}}^n - \sum_{i=1}^J \alpha_i \mathbf{u}^{n-i}}{\Delta t} = -\mathbf{N}_{k-1}^n, \quad (2.14a)$$

$$\frac{\tilde{\mathbf{u}}^n - \tilde{\mathbf{u}}^n}{\Delta t} = -\frac{\nabla p_k^n}{\rho_f}, \quad (2.14b)$$

$$\gamma \mathbf{u}_k^n - \frac{\tilde{\mathbf{u}}^n}{\Delta t} = \nu \nabla^2 \mathbf{u}_k^n, \quad (2.14c)$$

where

$$\mathbf{N}_{k-1}^n = (\mathbf{u}_{k-1}^n - \mathbf{w}^{n-1}) \cdot \nabla \mathbf{u}_{k-1}^n, \quad (2.15)$$

and

$$\mathbf{u}_k^n = \frac{\partial \boldsymbol{\eta}_k^n}{\partial t} \quad \text{on } \Sigma(t), \quad (2.16)$$

$$\frac{\partial p_k^n}{\partial \mathbf{n}_f} = -\rho_f \left(\frac{\partial^2 \boldsymbol{\eta}_k^n}{\partial t^2} + \nu \nabla \times \nabla \times \mathbf{u}_{k-1}^n + \mathbf{N}_{k-1}^n \right) \cdot \mathbf{n}_f \quad \text{on } \Sigma(t). \quad (2.17)$$

Here J denotes the time integration order, and α_i , γ are the corresponding coefficients of the J -th order backward differentiation formulas (Karniadakis and Sherwin, 2005). In (2.17), \mathbf{n}_f is the normal vector of fluid subdomain pointing outward on the interface $\Sigma(t)$.

Similar to the Navier–Stokes equation, at each time step the mesh velocity is obtained by solving the Laplace equation (2.12) with the spectral element method. The current configuration $\mathbf{x}(t)$ is updated from:

$$\frac{\mathbf{x}^n - \sum_{i=1}^J \hat{\alpha}_i \mathbf{x}^{n-i}}{\Delta t} = \sum_{i=1}^J \hat{\alpha}_i \mathbf{w}^{n-i}. \quad (2.18)$$

Here $\hat{\alpha}_i$ and $\hat{\alpha}_i$ are the coefficients for the corresponding time integration schemes, as given by Karniadakis et al. (1991). For more details about the fluid solver, we refer the interested readers to the works of Yu et al. (2013).

2.2.2. Structure (cylinder and fairing) solver

We discretize the structure system (2.7) in time with the Newmark scheme: for the object function $a(t)$, based on the current value a^n , previous time step values a^{n-1} , velocity approximation \dot{a}^{n-1} and acceleration approximation \ddot{a}^{n-1} , we can approximate the acceleration and velocity at the n -th step as

$$\dot{a}^n = \dot{a}^{n-1} + \Delta t \left((1 - D_1) \ddot{a}^{n-1} + D_1 \ddot{a}^n \right), \quad (2.19a)$$

$$\ddot{a}^n = \frac{1}{\Delta t^2 D_2} \left(a^n - a^{n-1} - \Delta t \dot{a}^{n-1} - \frac{\Delta t^2}{2} (1 - 2D_2) \ddot{a}^{n-1} \right), \quad (2.19b)$$

where we have used “.” to denote the approximated temporal derivative. Depending on the requirements of accuracy and stability, different values can be set for the parameters (D_1, D_2) . In the following, we will use the parameters $(D_1, D_2) = (0.5, 0.25)$ which lead to a second-order scheme. Substituting into (2.7), we obtain the discretized formulation for cylinder and fairing equations in the strongly coupled FSI system at time step n and subiteration step k :

$$m_c \left[(\ddot{f}_x)_k^n + a \left((\dot{\theta}_k^n)^2 \cos \theta_k^n + \ddot{\theta}_k^n \sin \theta_k^n \right) \right] + k_x \left[(f_x)_k^n - a \cos \theta_k^n \right] - (F_n)_k^n (\cos \beta_k^n + (f_c)_{k-1}^n \sin \beta_k^n) = (F_{chx})_{k-1}^n, \quad (2.20a)$$

$$m_c \left[(\ddot{f}_y)_k^n + a \left((\dot{\theta}_k^n)^2 \sin \theta_k^n - \ddot{\theta}_k^n \cos \theta_k^n \right) \right] + k_y \left[(f_y)_k^n - a \sin \theta_k^n \right] - (F_n)_k^n (\sin \beta_k^n - (f_c)_{k-1}^n \cos \beta_k^n) = (F_{chy})_{k-1}^n, \quad (2.20b)$$

$$m_f (\ddot{f}_x)_k^n + (F_n)_k^n (\cos \beta_k^n + (f_c)_{k-1}^n \sin \beta_k^n) = (F_{fmx})_{k-1}^n, \quad (2.20c)$$

$$m_f (\ddot{f}_y)_k^n + (F_n)_k^n (\sin \beta_k^n - (f_c)_{k-1}^n \cos \beta_k^n) = (F_{fmy})_{k-1}^n, \quad (2.20d)$$

$$I_f \ddot{\theta}_k^n - (F_n)_k^n \left[a \sin(\beta_k^n - \theta_k^n) - a (f_c)_{k-1}^n \cos(\beta_k^n - \theta_k^n) - R (f_c)_{k-1}^n \right] = (M_{fn})_{k-1}^n, \quad (2.20e)$$

where the hydrodynamic forces and angular momentum are updated from the following expressions:

$$\begin{pmatrix} (F_{chx})_{k-1}^n \\ (F_{chy})_{k-1}^n \end{pmatrix} = \int_{\Sigma(t)_c} \mathbf{n}_f \cdot [-p_{k-1}^n \mathbf{I} + 2\rho_f \nu (\nabla \mathbf{u}_{k-1}^n + (\nabla \mathbf{u}_{k-1}^n)^T)] ds, \quad (2.21)$$

$$\begin{pmatrix} (F_{fmx})_{k-1}^n \\ (F_{fmy})_{k-1}^n \end{pmatrix} = \int_{\Sigma(t)_f} \mathbf{n}_f \cdot [-p_{k-1}^n \mathbf{I} + 2\rho_f \nu (\nabla \mathbf{u}_{k-1}^n + (\nabla \mathbf{u}_{k-1}^n)^T)] ds, \quad (2.22)$$

$$(M_{fn})_{k-1}^n = \int_{\Sigma(t)_f} \mathbf{r}(\mathbf{x}) \times [-p_{k-1}^n \mathbf{I} + 2\rho_f \nu (\nabla \mathbf{u}_{k-1}^n + (\nabla \mathbf{u}_{k-1}^n)^T)] ds, \quad (2.23)$$

where $\Sigma(t)_c$ is the interface between fluid and cylinder, $\Sigma(t)_f$ is the interface between fluid and fairing, and $\mathbf{r}(\mathbf{x})$ is a vector pointing from \mathbf{x} to the fairing gravity center at the current configuration.

2.3. Fictitious FSI stabilization method

In industrial applications, the values of fairing rotational inertia I_f are generally very low. In this case, the convergence of partitioned procedure is problematic because of the so-called added-mass effect (Causin et al., 2005). When the added-mass effect is strong, due to the time lag between solid and fluid the energy balance of the coupling algorithm may be broken, rendering the simulations unstable unless special treatments are introduced in the FSI algorithm (Burman and Fernández, 2009; Förster et al., 2007; Badia et al., 2008; Yu et al., 2013). In this work, additional acceleration schemes are employed to enhance the convergence rate. To be more specific, the Aitken acceleration (Mok et al., 2001; Kuttler and Wall, 2008; Deparis et al., 2006) and the fictitious methods (Baek and Karniadakis, 2012; Yu et al., 2013) are used. The combination of these two approaches was shown to be successful in the previous study by Yu et al. (2013).

The main idea of the Aitken relaxation in the fluid solver (Mok et al., 2001; Borazjani et al., 2008) is to perform under-relaxation at each sub-iteration step. At time step n and subiteration step k , we obtain the results $\tilde{\mathbf{c}}_k^n$ from the unrelaxed ones \mathbf{c}_k^n and a relaxation parameter τ_k , based on the following rule:

$$\tilde{\mathbf{c}}_k^n = \tau_k \tilde{\mathbf{c}}_{k-1}^n + (1 - \tau_k) \mathbf{c}_k^n. \quad (2.24)$$

Here τ_k is updated according to the Aitken rule as described by Mok et al. (2001):

$$\tau_k = \tau_{k-1} + (\tau_{k-1} - 1) \frac{(\mathbf{Q}_{k-1} - \mathbf{Q}_k) \cdot \mathbf{Q}_k}{\|\mathbf{Q}_{k-1} - \mathbf{Q}_k\|^2} \quad \text{where } \mathbf{Q}_k = \tilde{\mathbf{c}}_{k-1}^n - \mathbf{c}_k^n. \quad (2.25a)$$

To obtain a better control on the convergence rate, we can set the relaxation parameter τ_k within a range $[\tau_{min}, \tau_{max}]$, depending on the specific applications (Baek and Karniadakis, 2012).

On the other hand, in the fictitious inertia method additional terms are introduced in (2.6) to balance the added-mass operators. At time step n and subiteration step k , the discretized moment equation for fairing (2.20e) is replaced by

$$I_f(1+f_i)\ddot{\theta}_k^n - (F_n)_k^n[a \sin(\beta_k^n - \theta_k^n) - a(f_c)_{k-1}^n \cos(\beta_k^n - \theta_k^n) - R(f_c)_{k-1}^n] = (M_{fh})_{k-1}^n + I_f f_i \ddot{\theta}_{k-1}^n, \quad (2.26)$$

where f_i is the fictitious inertia coefficient. Here we note that when the subiteration converges, we have $\ddot{\theta}_k^n \approx \ddot{\theta}_{k-1}^n$. Therefore, the scheme (2.26) with fictitious inertia method should converge to the same results as the original scheme of Eq. (2.20) at the end of each time step. Moreover, as discussed by Yu et al. (2013), the fictitious method works the best if it approximates an exact coupled algorithm, which happens when $I_f f_i$ is close to the actual added-mass operator. In the applications with complicated geometries such as the fairings here, we cannot obtain any reasonable analytical value for the optimal fictitious coefficient I_f . Therefore, we will investigate this optimal coefficient from numerical tests in Section 3.1.

In summary, at the n -th time step, we solve the FSI system following the fixed point algorithm:

1. Set

$$\text{(Solid)} \quad (f_x)_0^n = (f_x)^{n-1}, \quad (f_y)_0^n = (f_y)^{n-1}, \quad \theta_0^n = \theta^{n-1}, \quad \beta_0^n = \beta^{n-1}, \quad (F_n)_0^n = (F_n)^{n-1}, \quad (2.27a)$$

$$\text{(Fluid)} \quad \mathbf{u}_0^n = \mathbf{u}^{n-1}, \quad p_0^n = p^{n-1}. \quad (2.27b)$$

2. **for** $k = 1: k_{max}$, **do**

(a) (Solid) Solve the cylinder/fairing equations (2.26) with hydrodynamic forces generated as in (2.21) and (2.22) and hydrodynamic angular momentum as in (2.23), then update the cylinder/fairing results

$$((f_x)_k^n, (f_y)_k^n, \theta_k^n, \beta_k^n, (F_n)_k^n).$$

(b) (Solid) From $((f_x)_k^n, (f_y)_k^n, \theta_k^n, \beta_k^n, (F_n)_k^n)$, calculate the velocity and acceleration approximations based on the Newmark scheme (2.19a).

(c) (Solid) Generate $\dot{\eta}_k^n$ at the fluid–structure interface following (2.11) and approximate velocity approximation $\dot{\eta}_k^n$ and acceleration approximation $\ddot{\eta}_k^n$. Pass these approximations to the fluid solver.

(d) (Fluid) Update the velocity boundary condition $\mathbf{u}_k^n = \dot{\eta}_k^n$ and the pressure boundary condition $\partial p_k^n / \partial \mathbf{n}_f = -\rho_f (\ddot{\eta}_k^n + \nu \nabla \times \nabla \times \mathbf{u}_{k-1}^n + \mathbf{N}_{k-1}^n) \cdot \mathbf{n}_f$ at the interface.

(e) (Fluid) Solve the Navier–Stokes equation (2.14), and obtain updated velocity and pressure (\mathbf{u}_k^n, p_k^n) .

(f) (Fluid) Apply the Aitken relaxation on \mathbf{u}_k^n to obtain the relaxed velocity $\tilde{\mathbf{u}}_k^n$.

(g) (Fluid) Calculate the normal stress $-[-p_k^n \mathbf{1} + \rho_f \nu (\nabla \tilde{\mathbf{u}}_k^n + (\nabla \tilde{\mathbf{u}}_k^n)^T)] \mathbf{n}_f$ at the interface.

(h) (Fluid) Pass the normal stress at the interface to the structure solver.

(i) (Fluid) Check convergence: if

$$\|\tilde{\mathbf{u}}_k^n - \tilde{\mathbf{u}}_{k-1}^n\|, \quad \|p_k^n - p_{k-1}^n\| < \epsilon, \quad (2.28)$$

set $k = k_{max}$ and update the results as

$$\text{(Solid)} \quad (f_x)_k^n = (f_x)_k^n, \quad (f_y)_k^n = (f_y)_k^n, \quad \theta^n = \theta_k^n, \quad \beta^n = \beta_k^n, \quad (F_n)^n = (F_n)_k^n, \quad (2.29a)$$

$$\text{(Fluid)} \quad \mathbf{u}^n = \tilde{\mathbf{u}}_k^n, \quad p^n = p_k^n. \quad (2.29b)$$

Else, continue to the $(k+1)$ -th subiteration.

3. (Mesh) Update the mesh velocity boundary condition at the interface with $\mathbf{w}^n = \dot{\eta}^n$.

4. (Mesh) Obtain the mesh velocity \mathbf{w}^n by solving (2.12).

5. (Mesh) Update the mesh positions for the fluid subdomain using the numerical integration as in (2.18).

6. Go to time step $n+1$.

3. Numerical tests

In this section, we present a series of numerical tests on the fairings' suppression of vortex-induced vibrations, to validate the numerical method employed in this paper. With these tests, we aim to demonstrate the capability of our fictitious inertia method in stabilizing the fluid–structure interaction simulations, and to investigate the grid convergence by increasing the polynomial order of the spectral elements. On the smaller domain shown in the left plot of Fig. 2, we consider cases with two Reynolds numbers based on the cylinder diameter $D=1$: $Re=100$ and $Re=500$. All the simulations are performed with the physical and numerical parameters summarized in Table 1 unless stated otherwise. All the parameters are in non-dimensional units. Note that the mass ratio between cylinder and fairing is $m_c/m_f = 6$, which is consistent with the settings in industrial use.

Table 1
Non-dimensional parameters used in the numerical simulations.

Parameter	Value
Cylinder diameter D	1.0
Fairing circular part diameter	1.2
Free-stream velocity U	1.0
Cylinder natural frequency f_N	0.215
Reduced velocity $U^* = U/f_N D$	4.65
Cylinder mass m_c	6.0
Fairing mass m_f	1.0
Cylinder spring constant $k_x, k_y = 4\pi^2 m_c f_N^2$	10.949
Fairing rotational inertia I_f	0.6
Cylinder-fairing gravity center distance a	0.0851
Fluid density ρ_f	1.0
Element polynomial order	3

Table 2
Averaged subiteration number for VIV test for $C_f=0$. When $Re=100$, $\Delta t = 0.0025$; when $Re=500$, $\Delta t = 0.0005$.

Re=100													
f_i	0.0	0.5	1.0	1.5	2.0(opt)	2.5	3.0	4.0	5.0	7.0	10.0	15.0	
Avg subiter	No conv	13.8	10.1	8.6	7.7	7.9	8.0	8.0	8.1	8.2	8.3	8.6	
Re=500													
f_i	0.0	0.5	1.0	1.5	2.0	2.5(opt)	3.0	4.0	5.0	7.0	10.0	15.0	
Avg subiter	No conv	12.8	9.3	7.9	7.5	7.3	7.7	8.2	8.3	8.7	9.3	9.7	

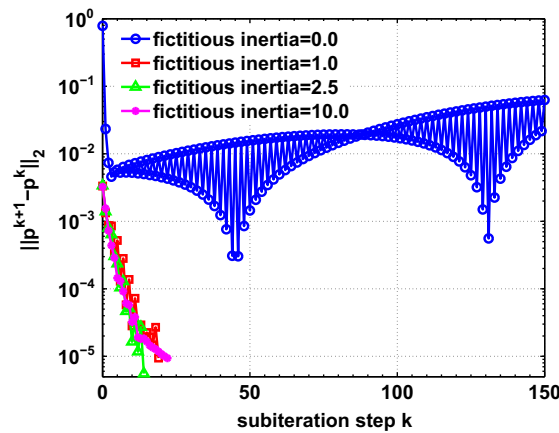


Fig. 4. Pressure change between each two subiteration steps in the first time step, when $Re=100$ and $C_f=0.0$. (For interpretation of the references to color in this figure caption, the reader is referred to the web version of this article).

3.1. Effect of fictitious method

Before performing the simulations, we first investigate the numerical performance of our fictitious inertia method and look for the optimal fictitious coefficient. With $C_f=0$, various values of f_i from 0.0 to 15.0 are tested and the averaged subiteration numbers needed for each f_i are compared in Table 2. The optimal fictitious coefficient f_i will be employed in all the simulations in Section 4.

3.1.1. $Re=100$

For the case $C_f=0$ and time step size $\Delta t = 0.0025$, we study systematically various values of f_i . To demonstrate the effect on accelerating the convergence, we take the average of subiteration numbers over one vortex shedding cycle (Strouhal

period) as a comparison index. In the first part of Table 2 we list these averaged subiteration numbers with different fictitious coefficients, where the value nearest to the optimal is marked by “(opt)”. To illustrate the effect of various fictitious coefficients more clearly, in Fig. 4 we plot the pressure changes of each subiteration in the first time step, for four cases with different f_j . From the results we can see that when no fictitious method is applied ($f_j=0.0$), the subiteration diverges in the first time step. Therefore, the fictitious inertia method helps stabilizing the simulations and accelerating the subiteration convergence. Among all cases, the best performance is achieved when $f_j=2.0$, which would be the coefficient we employ for all the $Re=100$ simulation cases in Section 4.

3.1.2. $Re=500$

For Reynolds number $Re=500$ cases, a smaller time step size $\Delta t=0.0005$ is employed to enhance the stability and accuracy. We also investigate the optimal fictitious coefficient through performing numerical tests for the $C_f=0$. The averaged subiteration numbers over one vortex shedding cycle (Strouhal period) are computed for f_j from 0.0 to 15.0, and listed in the second part of Table 2. Here the value nearest to the optimal is also marked with “(opt)”. Since the subiteration

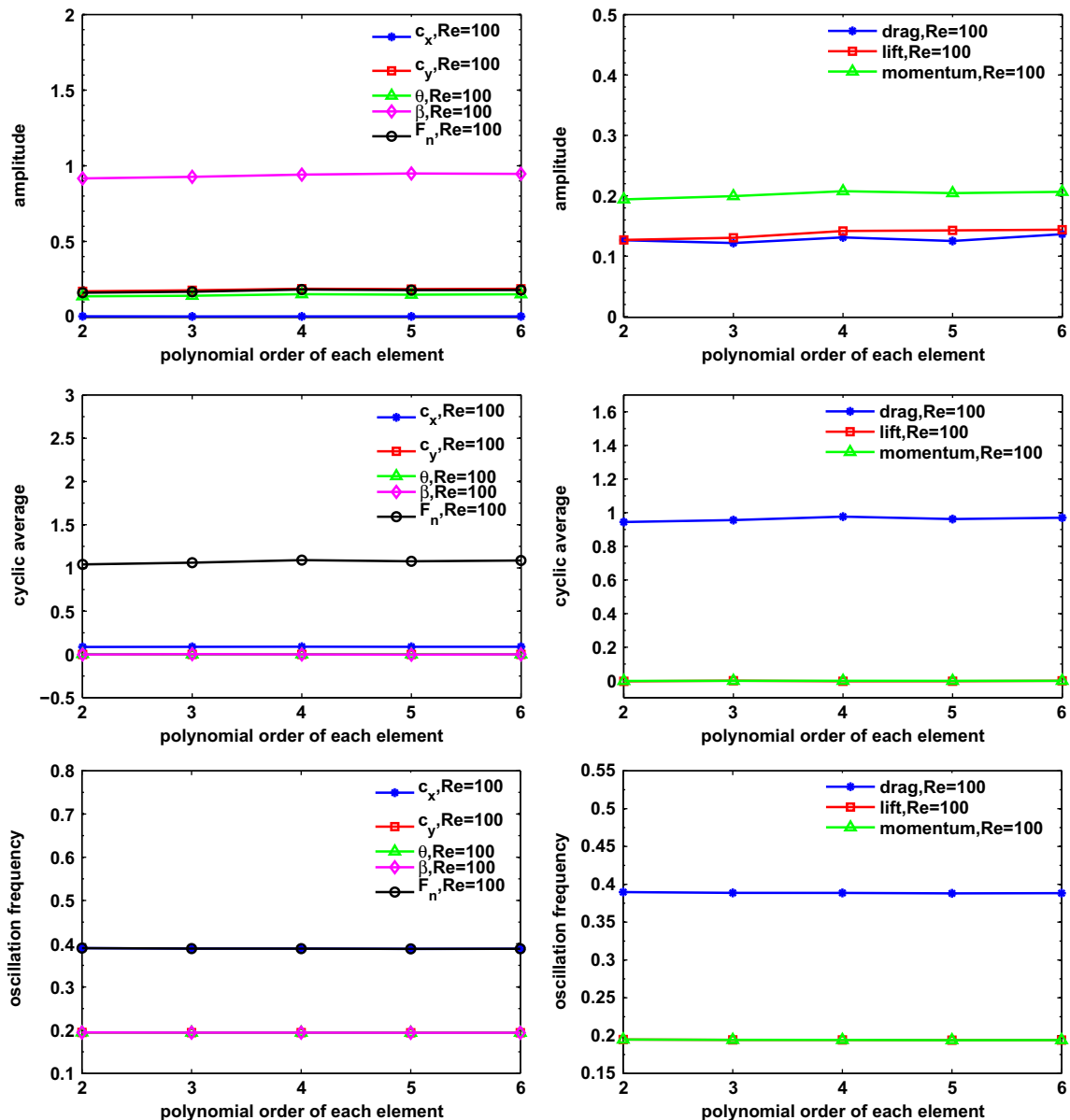


Fig. 5. Computational results from increasing polynomial orders with $C_f=0.25$ and $Re=500$, on the larger domain. Left column: motion variables (c_x , c_y , θ , β , F_n); right column: total hydrodynamic drag/lift forces and fairing angular momentum. Upper row: amplitudes of vibration in each cycle. Middle row: averages of cyclic response. Bottom row: frequencies of cyclic response. (For interpretation of the references to color in this figure caption, the reader is referred to the web version of this article.)

is not converged when $f_i=0.0$, in this higher Reynolds number case the fictitious inertia method is also required to stabilize the fluid–structure interaction simulations. On the other hand, the smallest subiteration number is obtained by $f_i=2.5$, which is close to the optimal fictitious coefficient for the $Re=100$ case. This implies that the added-mass operator does not change much with the increase of Reynolds number. In the remaining simulations of $Re=500$ cases, the fictitious inertia method with fictitious coefficient $f_i=2.5$ will be applied.

3.2. Grid convergence

We now study the grid convergence of the fairing simulation following the method described by Mittal and Kumar (2003), by comparing the results from elements with varying polynomial orders 2–6. Here the larger domain shown in Fig. 3 is employed, and all tests are on the case of $Re=500$ and $C_f=0.25$. The amplitudes of vibration, the averages and frequencies in each cycle are provided in the right column of Fig. 5 as functions of element order, with different colors and symbols representing the results of different variables of $(c_x, c_y, \theta, \beta, F_n)$. We can see that the responses from order 2 elements are almost the same as those from the order 6 elements, i.e., the p -refinement does not change much of the simulation results. On the other hand, in the left column of Fig. 5 we show the results of hydrodynamic forces and angular momentum, where the hydrodynamic forces are calculated as the total forces on the whole structure system including the fairing and cylinder, and the hydrodynamic angular momentum is calculated on the fairing only. Similarly, the results do not vary much while increasing the element polynomial order. Therefore in the rest of the current paper we are going to employ the third order elements for all simulations, since this grid convergence test shows that such a grid should have enough spacial resolution.

4. Simulation results

Before comparing the fairing performances from different values of C_f , we first study the typical VIV responses for the fairing-cylinder system over a range of cylinder natural frequencies $f_N = 0.5 - 0.1$, which corresponds to reduced velocities $U^* = 2.0 - 10.0$. At $Re=100$, $C_f=0.25$, the system amplitude and frequency responses are plotted as functions of increasing U^* in Fig. 6. We can observe similar results as those in the plain cylinder VIV cases (Williamson and Govardhan, 2004): the largest oscillation amplitudes are achieved when the reduced velocity U^* is around 4.65, and a departure from the fixed body shedding frequency 0.168 can be seen for the resultant oscillation frequency in the direction transverse to the flow.

Next we present the simulation results from various friction coefficient C_f from 0.0 to 0.5 to study the influence of rotational friction on the fairing effectiveness in suppressing VIV. Fig. 7 presents the instantaneous pressure coefficient contours and velocity vectors when the cylinder is crossing the centerline from bottom to top, i.e., when the transverse velocity of cylinder reaches the maximum. Here the pressure coefficient is defined with respect to the pressure at a upper stream point $(-5, 0)$ as

$$C_p(x, y) = \frac{2(p(x, y) - p(-5, 0))}{\rho_f U_\infty^2}$$

To provide a comparison and demonstrate the effects of fairing more clearly, Fig. 8 shows the instantaneous pressure coefficient contours and velocity vectors obtained from plain moving cylinder, i.e., without any fairing. In Figs. 9 and 10 we show trajectories of motions and forces along various values of friction coefficient, for $Re=100$ and $Re=500$, respectively, compared with the response of a plain cylinder (in red). The amplitudes of vibration, the averages and frequencies in each cycle are provided in Fig. 11 as functions of friction coefficient C_f for both $Re=100$ (in the left column) and $Re=500$ (in the right column), with different colors and symbols representing the results of different variables of $(c_x, c_y, \theta, \beta, F_n)$. Similarly, in Fig. 12 we show the results of hydrodynamic forces and angular momentum.

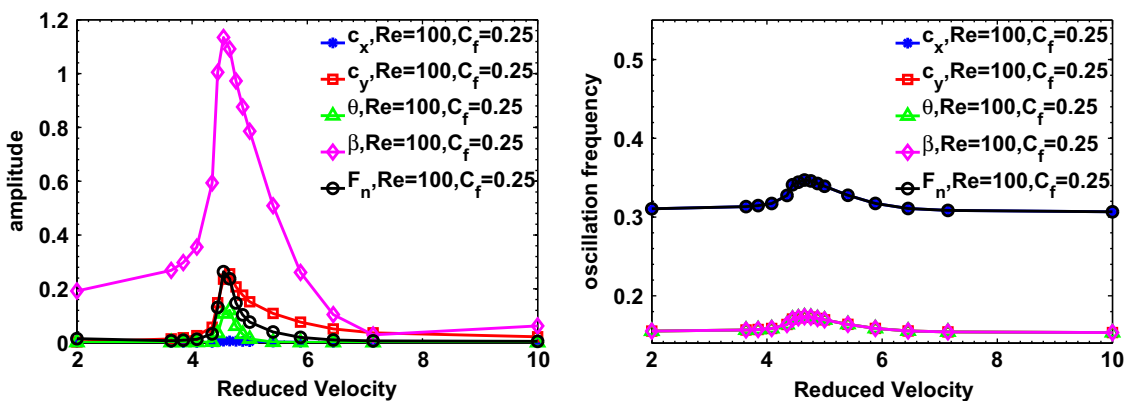


Fig. 6. VIV response of $(c_x, c_y, \theta, \beta, F_n)$ for the fairing-cylinder system for $Re=100$ and $C_f=0.25$, as functions of reduced velocities U^* . Left: amplitudes of vibration in each cycle. Right: frequencies of cyclic response. (For interpretation of the references to color in this figure caption, the reader is referred to the web version of this article.)

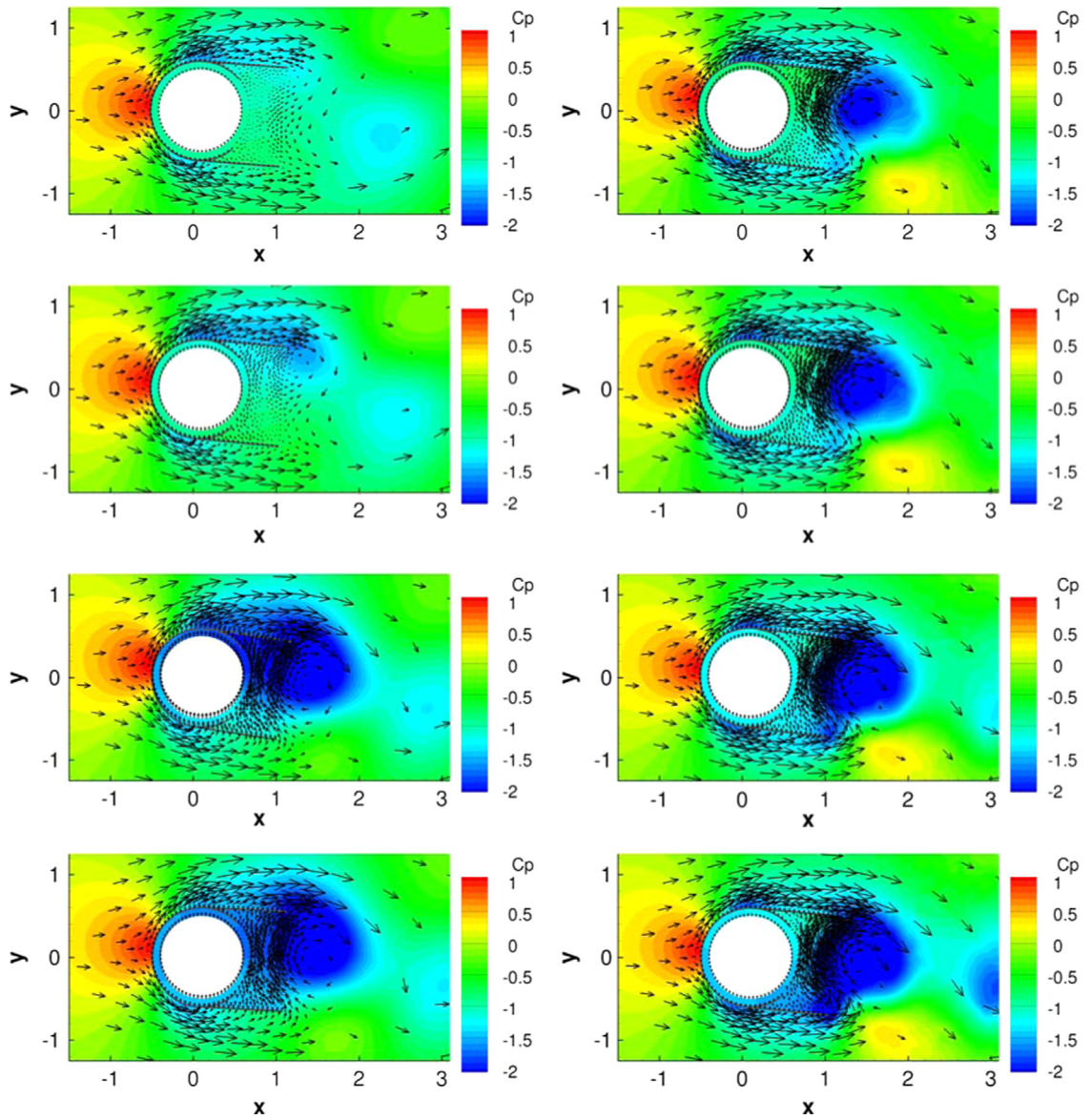


Fig. 7. Instantaneous pressure coefficient contours and velocity vectors for fairing cases, when the cylinder is crossing the centerline from bottom to top. Left column: $Re=100$; right column: $Re=500$ (small domain). First row: $C_f=0.0$; second row: $C_f=0.1$; third row: $C_f=0.2$; fourth row: $C_f=0.3$.

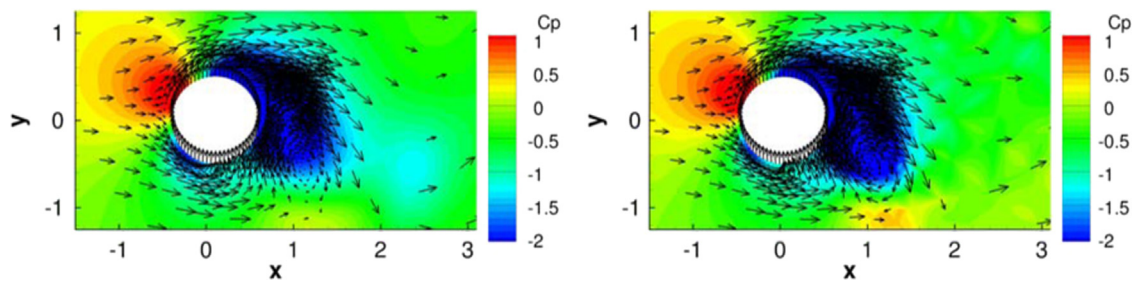


Fig. 8. Instantaneous pressure coefficient contours and velocity vectors for plain cylinder cases, when the cylinder is crossing the centerline from bottom to top. Left: $Re=100$; right: $Re=500$ (large domain).

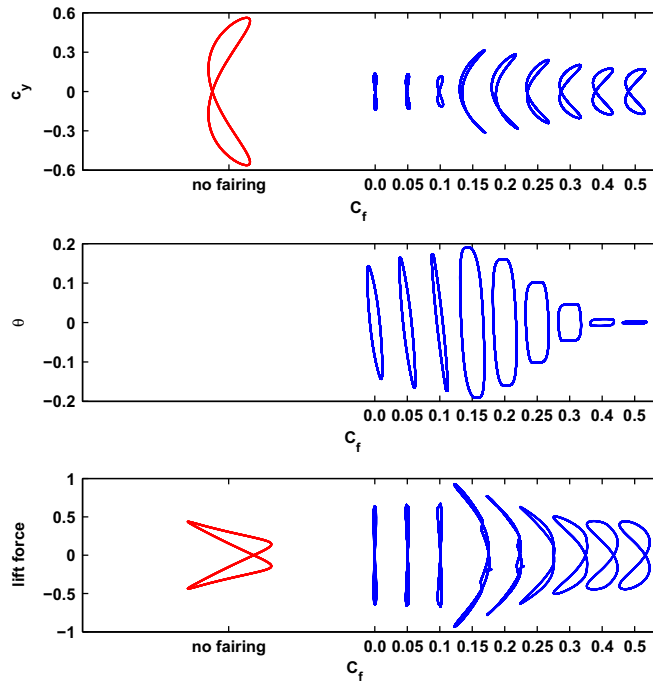


Fig. 9. Trajectories of motion and force when $Re=100$. The horizontal axis represents selected values of C_f and the trajectory centered at a specific value of C_f shows the computational results of that friction coefficient. Upper: $c_x - c_y$ trajectories. Middle: $\theta - \beta$ trajectories. Bottom: total hydrodynamic drag forces-lift forces trajectories. (For interpretation of the references to color in this figure caption, the reader is referred to the web version of this article.)

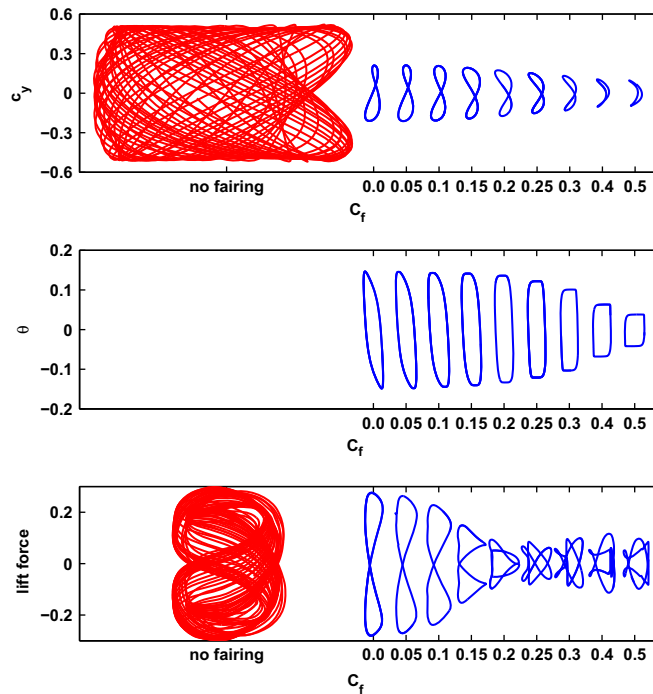


Fig. 10. Trajectories of motion and force when $Re=500$ (small domain). The horizontal axis represents selected values of C_f and the trajectory centered at a specific value of C_f shows the computational results of that friction coefficient. Upper: $c_x - c_y$ trajectories. Middle: $\theta - \beta$ trajectories. Bottom: total hydrodynamic drag forces-lift forces trajectories. (For interpretation of the references to color in this figure caption, the reader is referred to the web version of this article.)

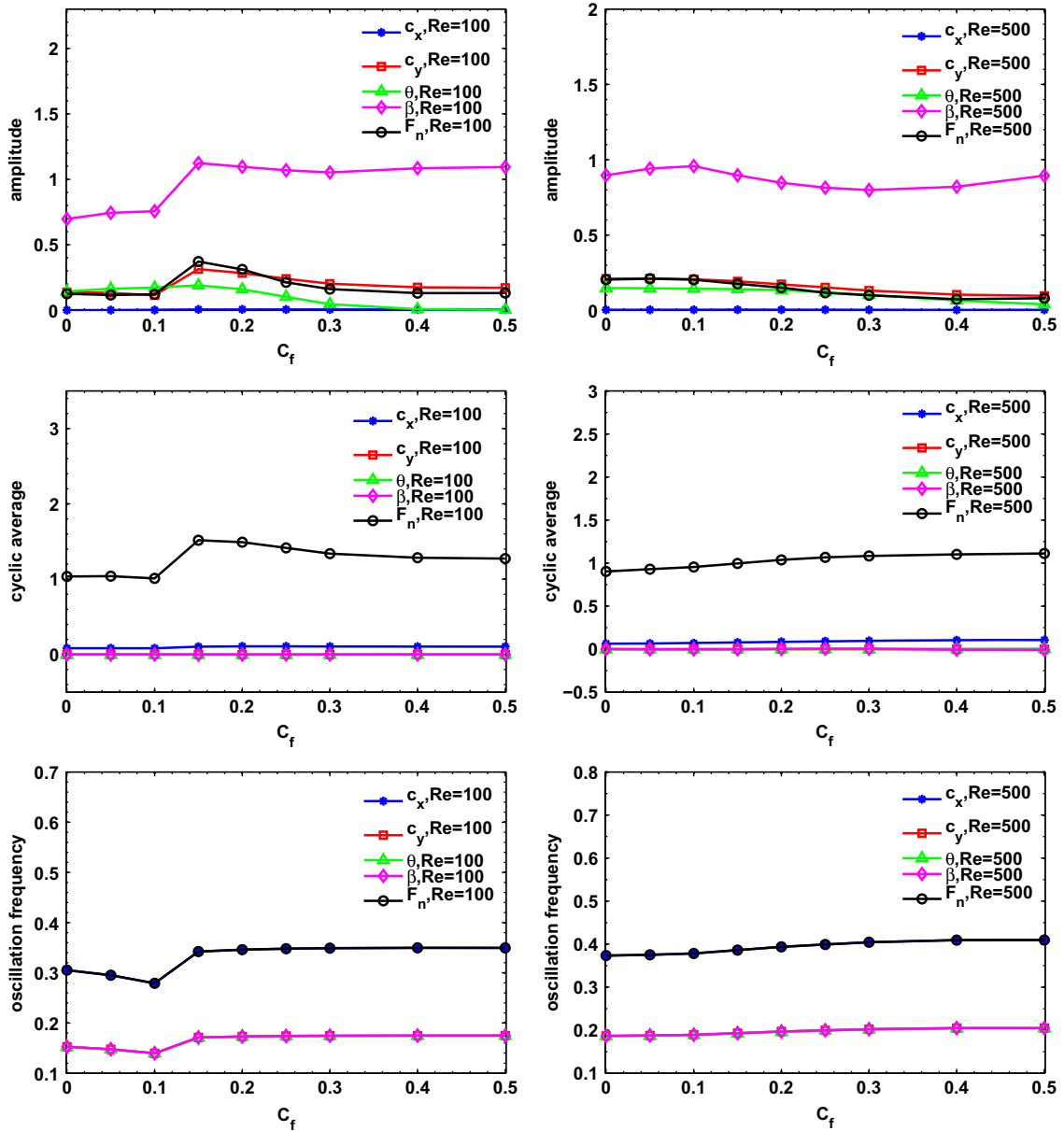


Fig. 11. Computational results of ($c_x, c_y, \theta, \beta, F_n$) from increasing C_f . Left column: $Re=100$; right column: $Re=500$ (small domain). Upper row: amplitudes of vibration in each cycle. Middle row: averages of cyclic response. Bottom row: frequencies of cyclic response. (For interpretation of the references to color in this figure caption, the reader is referred to the web version of this article.)

4.1. $Re=100$

Comparing the velocity vectors in the left column of Fig. 7 with the results from the plain cylinder in Fig. 8, it can be observed that in all the cases with fairing the instantaneous transverse velocities of cylinder are smaller than that from the plain cylinder simulation. Regarding the pressure coefficient contours, when $C_f=0.2$ the pressure contours show a region of lower pressure developed along the upper side of the upper fairing plate especially, which indicates a stronger transverse force in the same direction as the cylinder motion comparing with that in the lower C_f cases. As we further increase C_f to 0.3, there also exists a lower pressure region near the cylinder and fairing. However, this region is attached at the tip of the upper fairing plate instead of covering the whole upper side of the fairing plate as in the $C_f=0.2$ case. This suggests that the shear layers that stem from the cylinder are now attached to the tip of fairing plate, and this pattern has the effect of stabilizing the near wake flow. Therefore, the transverse force developed in the $C_f=0.3$ case should be smaller than that in the $C_f=0.2$ case. The above observations are further reinforced in Figs. 9 and 11. In the upper plot of Fig. 9 we can see that the cylinder motion trajectories with fairing show lower amplitudes of vibration for both the streamwise and transverse

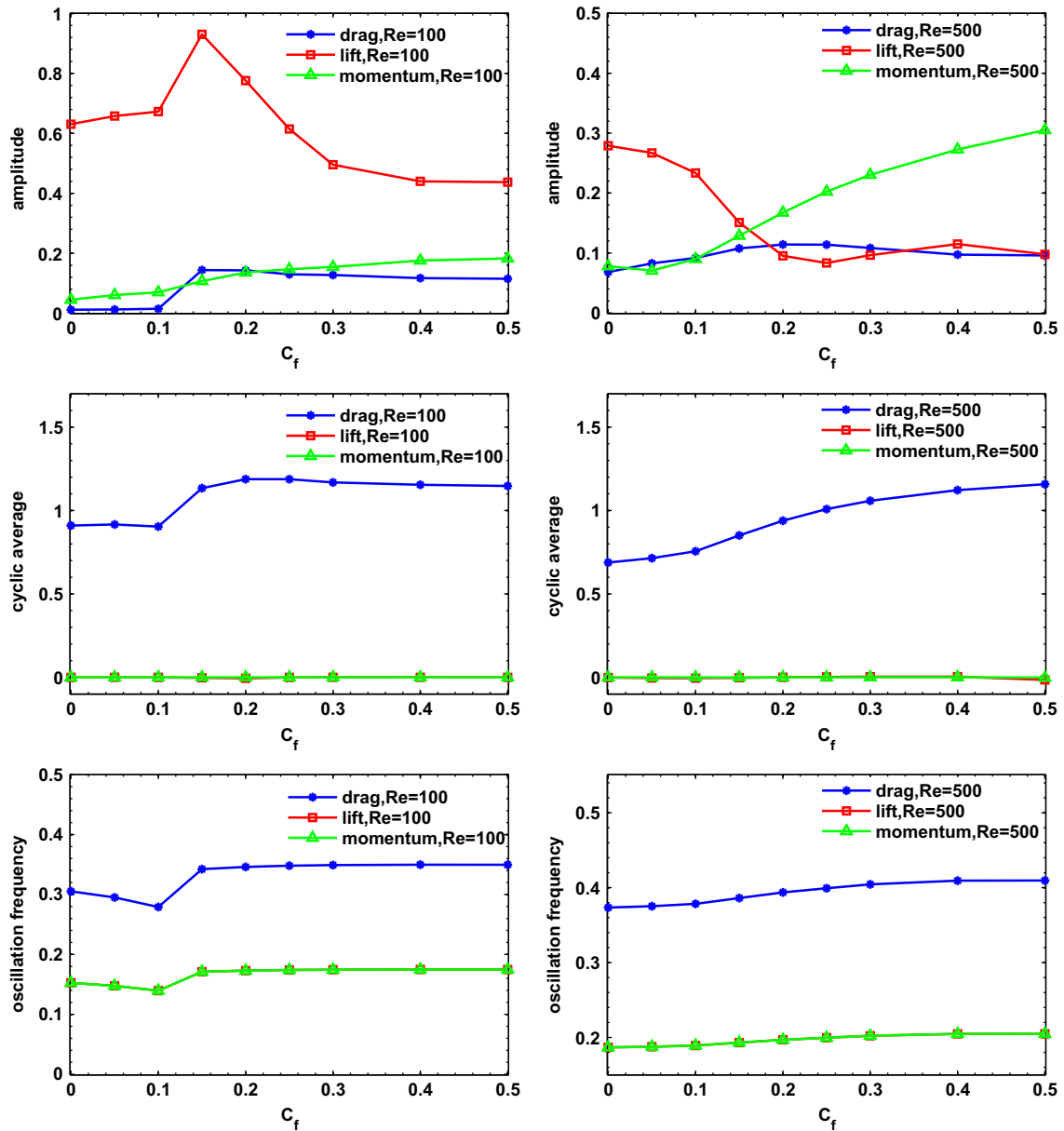


Fig. 12. Computational results of total hydrodynamic drag/lift forces and fairing angular momentum from increasing C_f . Left column: Re=100; right column: Re=500 (small domain). Upper row: amplitudes of vibration in each cycle. Middle row: averages of cyclic response. Bottom row: frequencies of cyclic response. (For interpretation of the references to color in this figure caption, the reader is referred to the web version of this article.)

responses than those for a plain cylinder. However, this is not evident from computing the hydrodynamic forces. Although in all cases the fairing helps reducing the amplitude of drag forces, when $C_f < 0.3$ the hydrodynamic lift forces with fairing are even higher than that computed for the plain cylinder. While comparing the effects of different C_f values, among all cases $C_f=0.0$ performs the best in suppressing VIV and reducing the drag force. On the other hand, in the left column of Fig. 11 it is especially worth noticing that when C_f is around 0.15–0.2, the amplitudes of vibration and the averages of all variables reach the maximum. Moreover, in the upper plot of Fig. 9 we can observe that only the $C_f=0.15$ and $C_f=0.2$ cases generates a non-symmetrical $c_x - c_y$ trajectory. Therefore, in this low Reynolds number case $C_f = 0.15 - 0.2$ seems to be a critical value for the dynamic responses.

In summary, when Re=100 the fairing in all cases helps in reducing the displacement responses and the hydrodynamic drag forces, but not the hydrodynamic lift forces applied on the cylinder and fairing. To achieve the best performance in VIV suppression and drag reduction, $C_f=0.0$ is the most effective choice. Moreover, there exists a critical value of the friction coefficient C_f around 0.15–0.2: when C_f is lower than this value, larger values of C_f are less effective in VIV suppression. On the other hand, when C_f exceeds this critical value, further increasing C_f will help more in suppressing the VIV.

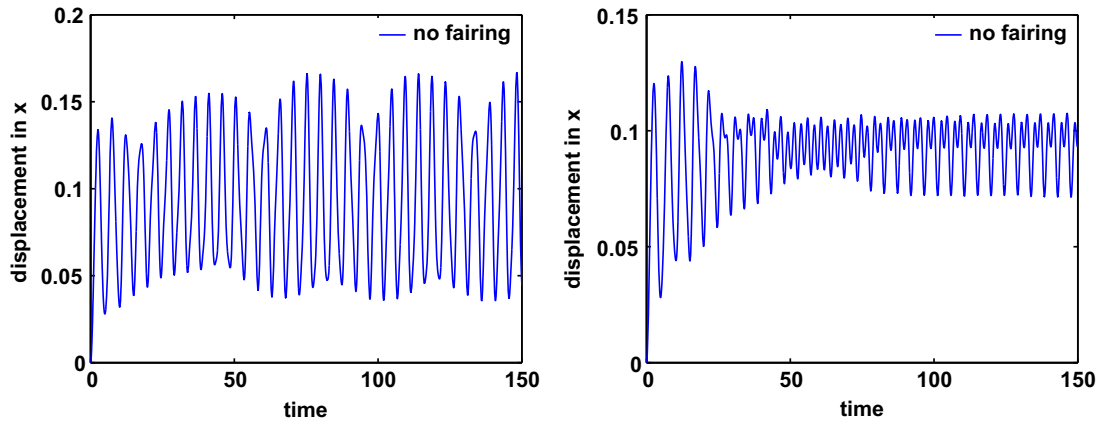


Fig. 13. Computational results of plain cylinder displacement in x direction when $Re=500$. Left: with smaller domain $([-5, 20] \times [-5, 5])$ we get a quasi-periodic flow; right column: with larger domain $([-10, 40] \times [-10, 10])$ a single frequency limit cycle emerges in the simulations.

4.2. $Re=500$ (small domain)

Similar to the results for $Re=100$, when $Re=500$ trajectories of motion and force for various values of friction coefficient are presented in Fig. 10. Compared with the trajectory of the plain cylinder (in red), the fairing is found to suppress not only the cylinder displacements but also the hydrodynamic forces. While considering the effect of different values of C_f , in the right column of Fig. 11 the computations of responses suggest that a higher C_f is generally more effective in suppressing VIV for the cylinder displacements and fairing rotational angle. In contrast to the findings in the $Re=100$ cases, there exists no obvious critical value of C_f in the $Re=500$ cases. The trajectory patterns are more complicated for all fairing cases when $Re=500$, as all the cylinder motion trajectories are non-symmetric. On the other hand, the motion trajectory in the plain cylinder case shows a more complicated behavior: a quasi-periodic flow occurs because of the secondary frequency in the x displacement time trace, as displayed in the left plot of Fig. 13. To investigate the cause, we increase the cylinder gap size from 10 to 20 and show the results in the right plot of Fig. 13: the secondary frequency disappears and the cylinder motion becomes periodic. Therefore, this secondary frequency is generated from the effect of the periodic boundary condition in the vertical direction i.e., the influences from neighboring cylinders. Therefore, the pressure contour and velocity vector results of plain cylinder case for $Re=500$ in Fig. 8 are generated from the simulation on the large domain as shown in Fig. 3. In the next section, we will further investigate the results from this larger domain. The comparison of the velocity vectors in Fig. 8 and those in Fig. 7 also implies that the fairing helps reducing the magnitudes of cylinder transverse velocities. Comparing the pressure coefficient contours at $Re=100$ to that at $Re=500$, we can see that when $Re=500$ the lower pressure regions are attached at the tip of the upper fairing plate, which is close to the pattern we observed in the $Re=100$, $C_f=0.3$ case. Therefore, we can expect that the transverse forces are reduced in the fairing cases. Moreover, in the $Re=500$ cases, when C_f increases the low pressure region expands more to the tip of the lower fairing plate, which indicates a smaller transverse force.

In summary, when $Re=500$ the fairing helps to reduce both the displacement responses and the hydrodynamic forces, and the device with higher C_f works more effectively. This finding is also consistent with the experiments in the works of Assi et al. (2009, 2011) where fairings with different designs were employed and tested.

4.3. $Re=500$ (large domain)

In this section, a larger domain as shown in Fig. 3 is employed, to diminish the influences of neighboring cylinder interactions and outflow boundary conditions. For the plain cylinder case, the amplitude of cylinder transverse displacement is slightly increased compared to the results from the smaller domain, namely from 0.516 to 0.575. Regarding the fairing cases, this larger domain also generates approximately 10% larger vibration amplitudes for $(c_x, c_y, \theta, \beta, F_n)$ and hydrodynamic forces. The increased rotational angle θ is problematic while updating the mesh in the arbitrary Lagrangian Eulerian (ALE) framework (2.12) for the cases with $C_f \leq 0.15$. As illustrated in the left plot of Fig. 14 where the simulation starts from developed flow around the static cylinder and fairing at time 0, it can be observed that the amplitude of rotational angle grows rapidly and reaches 0.24 at the time instant marked by a green circle. At that time instant, the right plot of Fig. 14 demonstrates the updated mesh generated from ALE, in which the mesh is greatly distorted near the fairing tips. The aspect ratios of the nearby elements become very small, which renders the simulation unstable. To resolve this problem, we note that our fictitious inertia method (2.26) can not only balance the added-mass effect, but also play as a relaxation for the rotational angle. When $C_f=0.15$, we take a large fictitious coefficient $I_f=200$ at the starting stage, then gradually decrease it to the optimal coefficient $I_f=2.5$ after a periodic fluctuation is reached. On the other hand, if we further investigate a smaller friction coefficient $C_f=0.1$, the amplitude of θ reaches $\theta=0.35$ at the starting stage. To stabilize this

case, a further larger fictitious coefficient I_f is required, which however greatly slows down the subiteration convergence as can be seen in Table 2. Fortunately, we are less interested in the small friction coefficient cases since they are less effective in suppressing VIV, as studied in the previous section. Therefore, in this section we concentrate on the simulation results for $C_f > 0.1$ cases.

To be consistent with the results in Fig. 8, we also define the pressure coefficient with respect to the pressure at $(-5, 0)$, and observe the same patterns as that in the corresponding cases on small domain. Similar as the plots for small domain results, in Fig. 15 we display the trajectories of motions and forces, and in Fig. 16 the amplitudes of vibration, the averages and frequencies are plotted as functions of C_f . Comparing these plots with the results in Figs. 7–12 in the last section, we can see that although the vibration amplitudes and trajectory patterns vary, the main observation in Section 4.2 still holds: fairings with larger C_f are generally more effective in suppressing both the cylinder motions and hydrodynamic forces.

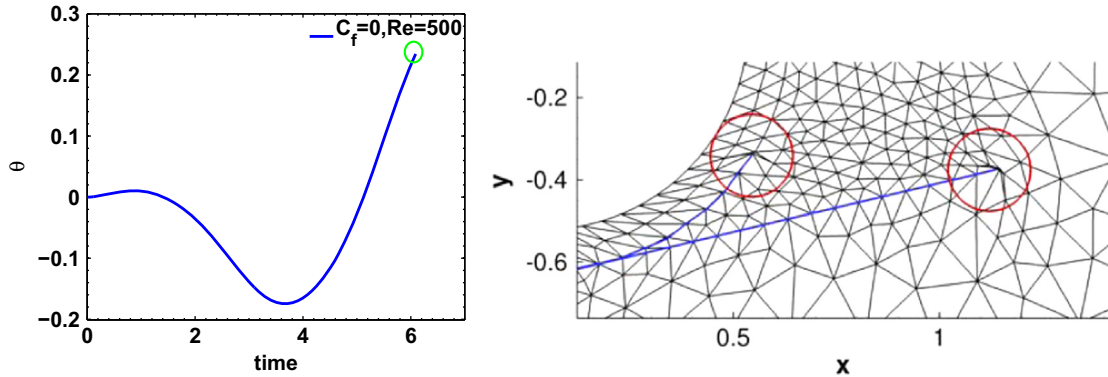


Fig. 14. Computational difficulty of the arbitrary Lagrangian Eulerian (ALE) framework (2.12) when using a larger domain. Left: time trace of rotational angle θ when $C_f=0$, at the starting stage; right column: distorted mesh generated from ALE, with low aspect ratio elements near the fairing tips circled by red. (For interpretation of the references to color in this figure caption, the reader is referred to the web version of this article.)

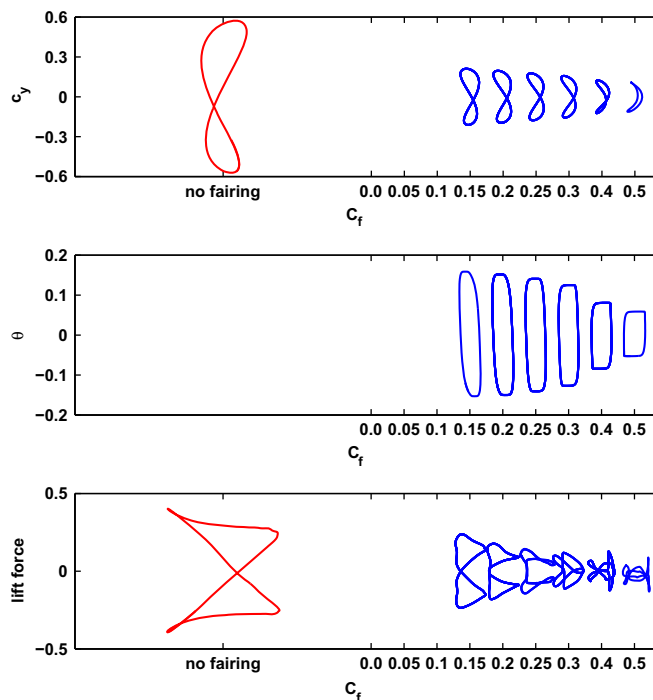


Fig. 15. Trajectories of motion and force with cylinder gap size 20 and $Re=500$. The horizontal axis represents selected values of C_f and the trajectory centered at a specific value of C_f shows the computational results of that friction coefficient. Upper: $c_x - c_y$ trajectories. Middle: $\theta - \beta$ trajectories. Bottom: total hydrodynamic drag forces–lift forces trajectories. (For interpretation of the references to color in this figure caption, the reader is referred to the web version of this article.)

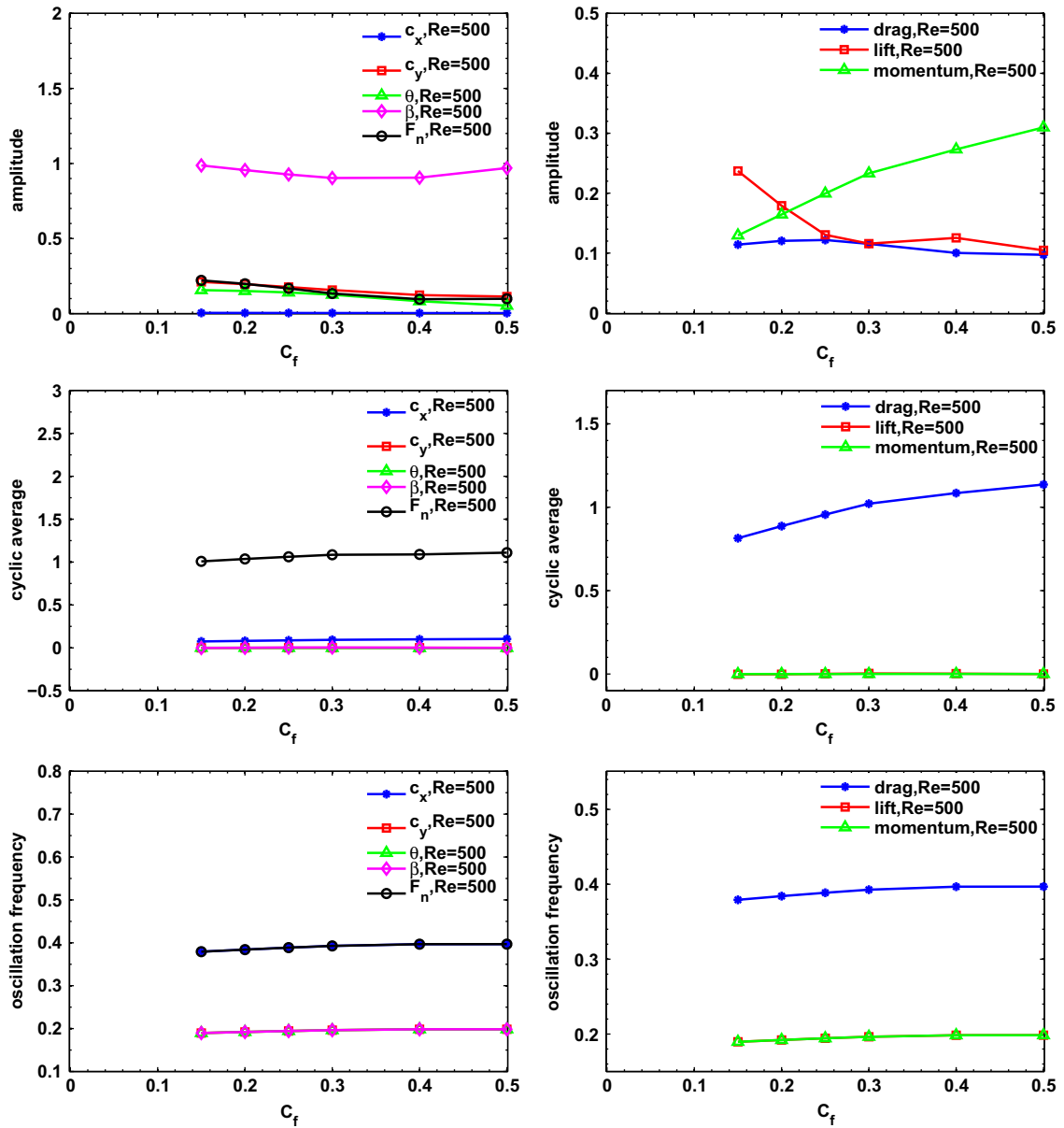


Fig. 16. Computational results from increasing C_f with cylinder gap size 20 and $Re=500$. Left column: motion variables (c_x , c_y , θ , β , F_n); right column: total hydrodynamic drag/lift forces and fairing angular momentum. Upper row: amplitudes of vibration in each cycle. Middle row: averages of cyclic response. Bottom row: frequencies of cyclic response. (For interpretation of the references to color in this figure caption, the reader is referred to the web version of this article.)

4.4. $Re=1000$ (2D and 3D simulations)

In this section, we study the three-dimensional (3D) flow around the fairing at $Re=1000$, and the results will be compared with those from the two-dimensional (2D) simulations. To generate a 3D fairing geometry, the 2D fairing geometry depicted in the right plot of Fig. 2 is extruded along the z -direction, by a length of three times of the cylinder diameter. The inflow and outflow boundary conditions are imposed similar to the 2D flow simulations, and the periodic boundary condition is applied along the z -direction. The simulations are preformed on the 3D extrusion of the large computational domain employed in Section 4.3, i.e., on a $[-10, 40] \times [-10, 10] \times [0, 3]$ computational domain. We first investigate the flow around a static fairing. In Fig. 17 we show the time traces of drag and lift force coefficients. A transition phase from 2D to 3D flow can be observed: when the time is around 34, both the drag and lift force coefficients drop quickly and the non-periodic traces begin to appear. Therefore, when the flow becomes 3D, using the 2D simulations tends to overestimate the hydrodynamic drag and lift forces acting on the static fairing. To further investigate the development of 3D effects, in Fig. 18 we display three instantaneous contours for the velocity in z -direction, at the $y=0$ plane, with the

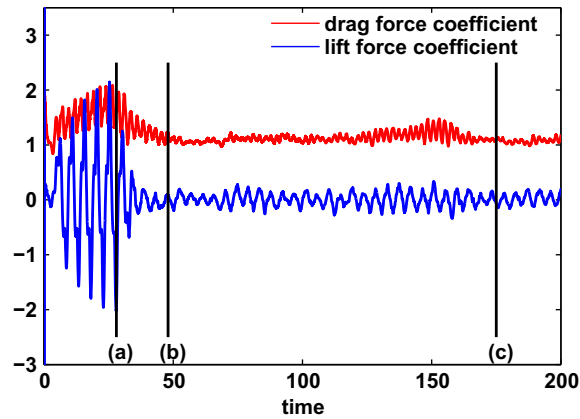


Fig. 17. Transition to three-dimensionality (static configuration): time traces of hydrodynamic drag and lift force coefficients on the fairing. (For interpretation of the references to color in this figure caption, the reader is referred to the web version of this article.)

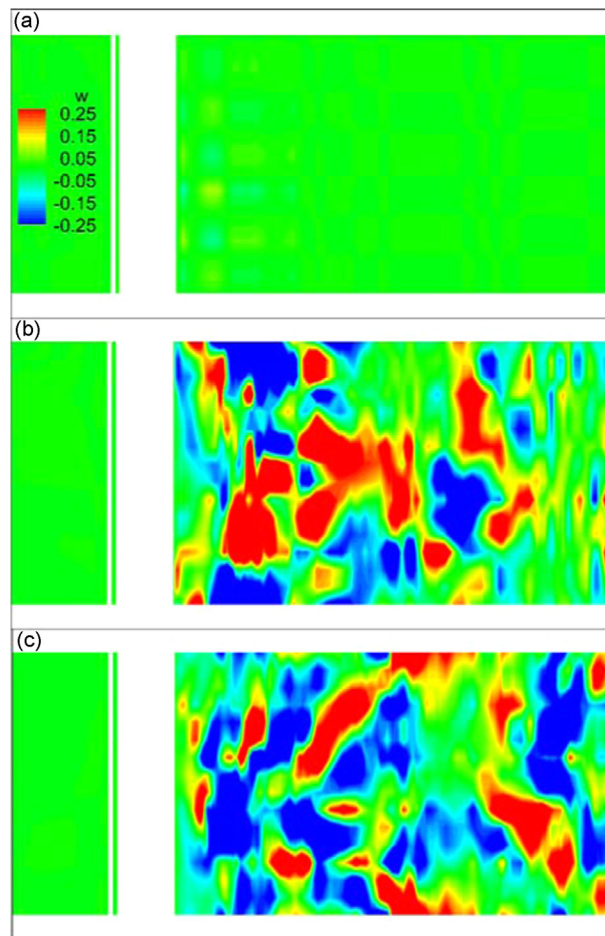


Fig. 18. Transition to three-dimensionality (static configuration): instantaneous velocity contour in the z -direction on the $y=0$ plane, where the two blank strips are in fact the cylinder and fairing. (a) time $t=28$, the flow is at 2D state; (b) time $t=48$, the flow is at transition state; (c) time $t=175$, the flow is at fully developed 3D state.

corresponding time instants marked by black lines in Fig. 17: (a) at 2D state, (b) at transition state and (c) at fully developed 3D state. We can see that in the transition state (b) the magnitudes of the velocity in z -direction are already of order $O(1)$. This observation further suggests that for $Re \geq 1000$ cases the 3D effects are non-negligible. Bearing this fact in mind, we now study the flow around a moving fairing, with varying friction coefficients C_f from 0 to 0.5. Here a large rotational inertia of fairing $I_f=6.0$ is adopted, to avoid the failure of ALE formulation caused by the significant fairing rotation observed in

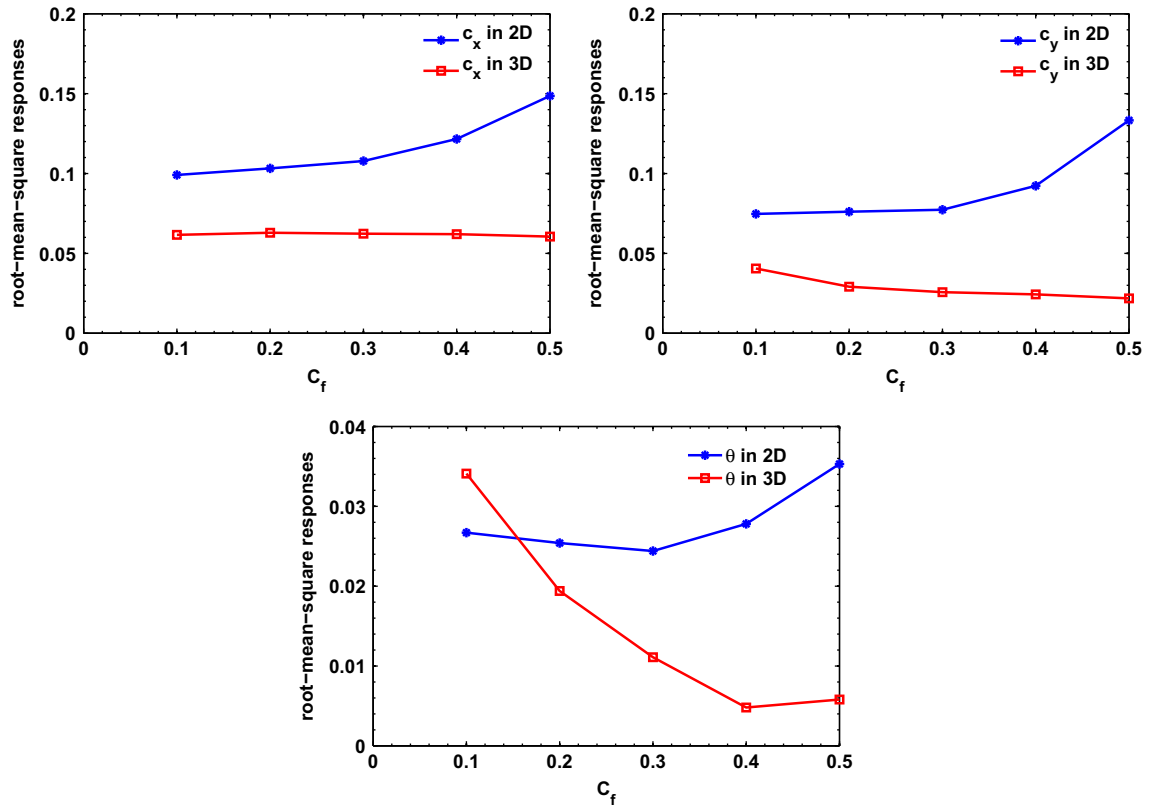


Fig. 19. Root-mean-square vibration responses for $Re=1000$, as functions of C_f . Upper left: cylinder displacement in the x direction. Upper right: cylinder displacement in the y direction. Lower: fairing rotation angle θ . (For interpretation of the references to color in this figure caption, the reader is referred to the web version of this article.)

Fig. 14. In 3D simulations, the vibration responses of fairing and cylinder are no longer periodic in time. To compare the simulation results between the 2D and 3D cases, we employ the root-mean-square of the vibration responses as the comparison index. In Fig. 19, the vibration responses of c_x , c_y and θ at $Re=1000$ are displayed, which shows that the 2D assumption increases the vortex shedding in the transverse direction and thereby results in higher vibration responses. Moreover, the 3D effects also change the trend of vibration responses from increasing friction coefficient C_f . In 2D simulations the root-mean-square of the resultant cylinder displacements and rotational angles increases when we use a larger C_f , suggesting that among all the tests, the case with lowest friction coefficient $C_f=0.1$ is the most effective one. On the other hand, 3D simulations show opposite results: the vibration responses reach their minimums when using large friction coefficient $C_f=0.5$, which is more consistent with the previous observations from experiments (Assi et al., 2009) and from our 2D simulation results in Section 4.3.¹

5. Conclusion

In this paper, we investigate the effectiveness of a specific model for a fairing geometry for VIV suppression used by the offshore oil industry in deepwater drilling, and numerically study its stabilization effect at different Reynolds numbers $Re = 100 - 1000$. The simulations were mostly conducted in two-dimensions, however, three-dimensional effects were also investigated for large Reynolds numbers $Re=500$ and 1000 . To resolve the numerical instabilities caused by the relatively low rotational inertia of the fairings, we extended the fictitious mass method to the fictitious inertia method, which is effective in stabilizing the FSI procedure in two ways: firstly, in balancing the added-mass effect, and secondly, when fairing rotational angle is as large as 0.25 , a large fictitious inertia I_f is needed for stabilization at the starting stage. Moreover, the fictitious inertia method can be easily implemented in open source codes, e.g., OpenFOAM (<http://www.openfoam.com>). The effects of varying the rotation friction between the riser and the fairing were investigated by comparing the vibration responses at different friction coefficients C_f . We found that at a low Reynolds number $Re=100$ there exists a critical value of friction coefficient C_f , around which large oscillations and non-symmetric trajectories occur. On the other hand, at $Re=500$ a

¹ To complete the investigation, we have also tested the 3D simulations for $Re=500$ and obtained almost the same results as what illustrated in Section 4.3. Here we omit the details to avoid redundancy.

different behavior emerges, i.e., VIV are suppressed continuously as C_f increases. When we further increased the Reynolds number to $Re = 1000$, three-dimensionality becomes important and the vibration amplitudes are two to three times smaller than their two-dimensional counterparts. Regarding the numerical aspects, we also found that a small computational domain, i.e. gap size between cylinders, might lead to a quasi-periodic result for the plain cylinder case, hence a larger domain is required to diminish the influence of periodic boundary conditions. However, in larger domain simulations, the main observations on fairing performance still hold.

In ongoing work we address high Reynolds number flow simulations, e.g., $Re = 10\,000$, which cannot be easily done with direct numerical simulations (DNS) and large-eddy simulations (LES) are required. In particular we investigate the effect of fairings which are non-continuous along the span of cylinder. Preliminary results suggest that the gap between adjacent fairing segments may have a significant effect in further reducing VIV but also the drag force and may totally suppress the vortex street, hence eliminating VIV all together. We will report a systematic study from these simulations in a future publication.

Acknowledgements

We would like to acknowledge partial support by the AFOSR FA9550-12-1-0463 and by the CHEVRON-MIT Agreement for PDEP CW819969.

Appendix A. Expression for coefficient of friction between the cylinder and fairing

To evaluate the relative velocity of fairing with respect to the cylinder, we consider the expressions of cylinder/fairing velocities at the contact point C. Since the cylinder does not rotate, every point on it has the same velocity as CG_c . Therefore, the tangential velocity of point C on the cylinder can be expressed as

$$\frac{\partial c_x}{\partial t} \sin \beta - \frac{\partial c_y}{\partial t} \cos \beta. \quad (\text{A.1})$$

On the other hand, now we consider the fairing side. Along the x direction, we have the velocity of fairing gravity center CG_f as $\partial f_x / \partial t$, the relative velocity of CG_c to CG_f as $a(\partial \theta / \partial t) \sin \theta$, and the relative velocity of contact point to CG_c as $R(\partial \theta / \partial t) \sin \beta$. Therefore, the velocity of point C along x direction is

$$\frac{\partial f_x}{\partial t} + a \frac{\partial \theta}{\partial t} \sin \theta + R \frac{\partial \theta}{\partial t} \sin \beta, \quad (\text{A.2})$$

and the velocity along the y direction can be similarly written as

$$\frac{\partial f_y}{\partial t} - a \frac{\partial \theta}{\partial t} \cos \theta - R \frac{\partial \theta}{\partial t} \cos \beta. \quad (\text{A.3})$$

Based on (A.2) and (A.3), we have the tangential velocity of point C on the fairing as

$$\left(\frac{\partial f_x}{\partial t} + a \frac{\partial \theta}{\partial t} \sin \theta + R \frac{\partial \theta}{\partial t} \sin \beta \right) \sin \beta - \left(\frac{\partial f_y}{\partial t} - a \frac{\partial \theta}{\partial t} \cos \theta - R \frac{\partial \theta}{\partial t} \cos \beta \right) \cos \beta. \quad (\text{A.4})$$

Combining (A.1) with the geometry relation (2.4), we can rewrite the tangential velocity expression on the cylinder side as

$$\left(\frac{\partial f_x}{\partial t} + a \frac{\partial \theta}{\partial t} \sin \theta \right) \sin \beta - \left(\frac{\partial f_y}{\partial t} - a \frac{\partial \theta}{\partial t} \cos \theta \right) \cos \beta. \quad (\text{A.5})$$

Subtracting (A.5) from the tangential velocity on the fairing side (A.4), we have the relative tangential velocity of fairing to cylinder at point C as $R(\partial \theta / \partial t)$. Therefore, the coefficient of friction between the cylinder and fairing should be proportional to the sign function of $\partial \theta / \partial t$. Note that $\text{sgn}(\partial \theta / \partial t)$ is not a C^1 function since it has a jump when $\partial \theta / \partial t = 0$. In the numerical simulations, this formulation might cause problems known as the Gibbs phenomena. Therefore, we employ a smoothed expression for f_c as

$$f_c = -C_f \text{sgn} \left(\frac{\partial \theta}{\partial t} \right) \exp \left(\frac{-0.001}{\left| \frac{\partial \theta}{\partial t} \right|} \right)$$

in all the numerical simulations.

References

- Assi, G., Bearman, P., Kitney, N., Tognarelli, M., 2010. Suppression of wake-induced vibration of tandem cylinders with free-to-rotate control plates. *Journal of Fluids and Structures* 26 (7), 1045–1057.
- Assi, G.R., Bearman, P.W., Tognarelli, M.A., Rodrigues, J.R., 2011. The effect of rotational friction on the stability of short-tailed fairings suppressing vortex-induced vibrations. In: Proceedings of the 30th International Conference on Ocean, Offshore and Arctic Engineering, OMAE2011. Rotterdam, The Netherlands.

- Assi, G.R.S., Bearman, P.W., Kitney, N., 2009. Low drag solutions for suppressing vortex-induced vibration of circular cylinders. *Journal of Fluids and Structures* 25 (4), 666–675.
- Astorino, M., Chouly, F., Fernández, M.A., 2009. Robin based semi-implicit coupling in fluid–structure interaction: stability analysis and numerics. *SIAM Journal of Scientific Computing* 31 (6), 4041–4065.
- Badia, S., Nobile, F., Vergara, C., 2008. Fluid–structure partitioned procedures based on Robin transmission conditions. *Journal of Computational Physics* 227 (14), 7027–7051.
- Baek, H., Karniadakis, G.E., 2009. Suppressing vortex-induced vibrations via passive means. *Journal of Fluids and Structures* 25 (5), 848–866.
- Baek, H., Karniadakis, G.E., 2011. Sub-iteration leads to accuracy and stability enhancements of semi-implicit schemes for the Navier–Stokes equations. *Journal of Computational Physics* 230 (12), 4384–4402.
- Baek, H., Karniadakis, G.E., 2012. A convergence study of a new partitioned fluid–structure interaction algorithm based on fictitious mass and damping. *Journal of Computational Physics* 231 (2), 629–652.
- Borazjani, I., Ge, L., Sotiropoulos, F., 2008. Curvilinear immersed boundary method for simulating fluid–structure interaction with complex 3d rigid bodies. *Journal of Computational Physics* 227 (16), 7587–7620.
- Burman, E., Fernández, M.A., 2007. Stabilized explicit coupling for fluid–structure interaction using Nitsche's method. *Comptes Rendus Mathématique* 345 (8), 467–472.
- Burman, E., Fernández, M.A., 2009. Stabilization of explicit coupling in fluid–structure interaction involving fluid incompressibility. *Computer Methods in Applied Mechanics and Engineering* 198 (5–8), 766–784.
- Causin, P., Gerbeau, J.F., Nobile, F., 2005. Added-mass effect in the design of partitioned algorithms for fluid–structure problems. *Computer Methods in Applied Mechanics and Engineering* 194 (42–44), 4506–4527.
- Cimbala, J.M., Garg, S., 1991. Flow in the wake of a freely rotatable cylinder with splitter plate. *AIAA Journal* 29 (6), 1001–1003.
- Degroote, J., 2011. On the similarity between Dirichlet–Neumann with interface artificial compressibility and Robin–Neumann schemes for the solution of fluid–structure interaction problems. *Journal of Computational Physics* 230 (17), 6399–6403.
- Degroote, J., Swillens, A., Bruggeman, P., Haelterman, R., Segers, P., Vierendeels, J., 2010. Simulation of fluid–structure interaction with the interface artificial compressibility method. *International Journal for Numerical Methods in Biomedical Engineering* 26 (3–4), 276–289.
- Deparis, S., Discacciati, M., Quarteroni, A., 2006. A domain decomposition framework for fluid–structure interaction problems. In: Groth, C., Zingg, D.W. (Eds.), *Computational Fluid Dynamics 2004*, Springer, Berlin, Heidelberg, pp. 41–58.
- Dong, S., Triantafyllou, G.S., Karniadakis, G.E., 2008. Elimination of vortex streets in bluff-body flows. *Physical Review Letters* 100 (20), 204501.
- Every, M.J., King, R., Weaver, D.S., 1982. Vortex-excited vibrations of cylinders and cables and their suppression. *Ocean Engineering* 9 (2), 135–157.
- Förster, C., Wall, W.A., Ramm, E., 2007. Artificial added mass instabilities in sequential staggered coupling of nonlinear structures and incompressible viscous flows. *Computer Methods in Applied Mechanics and Engineering* 196 (7), 1278–1293.
- Hughes, T.J.R., Liu, W.K., Zimmermann, T.K., 1981. Lagrangian–Eulerian finite element formulation for incompressible viscous flows. *Computer Methods in Applied Mechanics and Engineering* 29 (3), 329–349.
- Karniadakis, G.E., Israeli, M., Orszag, S., 1991. High-order splitting methods for the incompressible Navier–Stokes equations. *Journal of Computational Physics* 97 (2), 414–443.
- Karniadakis, G.E., Sherwin, S.J., 2005. In: *Spectral/hp Element Methods for Computational Fluid Dynamics (Numerical Mathematics and Scientific Computation)* 2nd edition Oxford University Press, Oxford.
- Korkischko, I., Meneghini, J., 2010. Experimental investigation of flow-induced vibration on isolated and tandem circular cylinders fitted with strakes. *Journal of Fluids and Structures* 26 (4), 611–625.
- Kuttler, U., Wall, W.A., 2008. Fixed-point fluid–structure interaction solvers with dynamic relaxation. *Computational Mechanics* 43 (1), 61–72.
- Mittal, S., Kumar, B., 2003. Flow past a rotating cylinder. *Journal of Fluid Mechanics* 476, 303–334.
- Mok, D., Wall, W., Ramm, E., 2001. Accelerated iterative substructuring schemes for instationary fluid–structure interaction, In: *First MIT Conference on Computational Fluid and Solid Mechanics*, Elsevier, Cambridge, MA, USA.
- Owen, J.C., Bearman, P.W., Szweczyk, A.A., 2001. Passive control of VIV with drag reduction. *Journal of Fluids and Structures* 15 (34), 597–605.
- Roux, F.X., Garaud, J.D., 2009. Domain decomposition methodology with Robin interface matching conditions for solving strongly coupled fluid–structure problems. *International Journal for Multiscale Computational Engineering* 7 (1), 29–38.
- Williamson, C.H.K., Govardhan, R., 2004. Vortex-induced vibrations. *Annual Review of Fluid Mechanics* 36, 413–455.
- Yu, Y., Baek, H., Karniadakis, G.E., 2013. Generalized fictitious methods for fluid–structure interactions: analysis and simulations. *Journal of Computational Physics* 245 (0), 317–346.
- Zdravkovich, M.M., 1981. Review and classification of various aerodynamic and hydrodynamic means for suppressing vortex shedding. *Journal of Wind Engineering and Industrial Aerodynamics* 7 (2), 145–189.